



# From melt- to crystal-rich magmatic systems during rift localization: Insights from mineral chemistry in Central Afar (Ethiopia)

Gianmaria Tortelli<sup>1,2</sup> · A. Gioncada<sup>2</sup> · C. Pagli<sup>2</sup> · E. Braschi<sup>3</sup> · E. F. Gebru<sup>4,5</sup> · D. Keir<sup>1,6</sup>

Received: 24 April 2024 / Accepted: 16 August 2024 / Published online: 5 September 2024  
© The Author(s) 2024

## Abstract

Magmatism plays a key role in accommodating and localizing extension during continental breakup. However, how the crustal magmatic systems evolve at the continental-ocean transition is poorly understood. We address these questions by studying the evolution of the magmatic system in the rift of Central Afar (Ethiopia), currently marking the transition from continental rifting to oceanic spreading. We focus on the voluminous and widespread Upper Stratoid Series (2.6–1.1 Ma) and the following Central Afar Gulf Series (1.1–0.6 Ma), the latter corresponding to localization of volcanism in narrow magmatic segments. We carried out the first systematic study of major and trace element mineral chemistry for these two Series and integrated it with geothermobarometry estimates and geochemical modeling, to reconstruct the evolution of the magmatic system architecture during rift localization. The Upper Stratoid magmas evolved by fractional crystallization in a melt-rich, moderately zoned, middle-lower crustal (10–18 km) magmatic system, from where they rose directly to the surface. Polybaric plagioclase convection and dissolution of a plagioclase-rich crystal mush is recorded in the phenocryst texture and chemistry. The Central Afar Gulf magmas evolved at similar depth in a more complex and dynamic storage system, with magma rising and mixing through multiple, relatively small, crystal-rich and interconnected reservoirs. Our study documents the transition during the continental breakup, from an overall stable and melt-rich magmatic system feeding the voluminous and homogeneous Upper Stratoid eruptions to a more dynamic, interconnected and crystal-rich situation feeding small-volume eruption while the rift localizes.

**Keywords** Afar · Magma plumbing system · Plagioclase · Rift evolution · Stratoid series · Continental breakup

## Introduction

The changes in magmatic system architecture during rifting are linked to the evolution of magma intrusion and volcanism in space and time (Su et al. 2021; Nicotra et al. 2021; Hutchison et al. 2018; Caracciolo et al. 2023). Volcanic activity can change drastically during rifting (Storch et al. 2020; Franceschini et al. 2020; Pouclet et al. 2018; Shillington et al. 2009; Brune et al. 2023) due to variation in mantle source melting, extension rate or volatile release (Muirhead et al. 2016; White and McKenzie 1989; White 1992). Bimodal volcanism has been observed in several Continental Flood Basalt (CFB) eruptions, typically taking place at the beginning of the continental breakup process (Natali et al. 2011; Webb et al. 2019; Ukstins et al. 2002). During subsequent rift evolution, the nature of the magmatism is also variable in erupted volumes and composition, alternating between mafic- and silicic-dominated volcanism (Rooney 2020a; Goswami et al. 2020; Dostal et al. 2017).

---

Communicated by Dante Canil.

✉ Gianmaria Tortelli  
gianmaria.tortelli@unifi.it

<sup>1</sup> Dipartimento di Scienze della Terra, Università degli Studi di Firenze, Via G. La Pira, 4, Florence 50121, Italy

<sup>2</sup> Dipartimento di Scienze della Terra, Università di Pisa, Via Santa Maria, 53, Pisa 56126, Italy

<sup>3</sup> CNR, IGG, sezione di Firenze, Via G. La Pira, 4, Firenze 50121, Italy

<sup>4</sup> Department of Geosciences, University of Fribourg, Chemin du Musée 6, Fribourg 1700, Switzerland

<sup>5</sup> School of Earth Sciences, Addis Ababa University, P. O. Box, 1176, Addis Ababa, Ethiopia

<sup>6</sup> School of Ocean and Earth Science, University of Southampton, European Way, Southampton SO14 3ZH, UK

Taking as an example the Ethiopian rift, continental rifting is initially associated with large-scale silicic volcanic events (Rooney 2020b; Wolfenden et al. 2005; Stab et al. 2016) followed by widespread fissural basaltic volcanism (Stab et al. 2016; Tortelli et al. 2022; Rooney 2020b) then by silicic central volcanism (Lahitte et al. 2003a), and lastly by localized volcanism and intrusion in magmatic segments (Mohr et al. 1978; Ebinger and Casey 2001; Siegburg et al. 2018).

In the last few years, several lines of evidence suggest that vertically stacked mush-magma-host rock magmatic systems exist in different geological settings (Cashman et al. 2017; Sparks et al. 2019; Neave et al. 2013; Caracciolo et al. 2023; Biggs et al. 2021; Chambers et al. 2021). Studies of the magmatic system during rift evolution suggest a progressive shallowing of the magma reservoirs (Fitton et al. 1998; Fowler et al. 2004). The magmatic system architecture of the most recent stage of the rifting process (magmatic segments) are well studied and reasonably well understood. For example, the seismic velocity and anisotropic structure of the rift valley crust suggests the plumbing system beneath the magmatic segments transitions from sill- to dyke-dominated storage mechanism as the rift widens (Chambers et al. 2021). Petrological constraints show this is associated with reservoir shallowing, decrease in magma storage time, and increase in erupted volumes of basaltic lava (Hutchison et al. 2018). However, the magmatic systems architecture of the rift prior, and leading up to, the localized volcanism in the magmatic segments is still poorly understood. In order to address this, in this work we use mineral chemistry data of a range of volcanic rocks from the Afar rift, at the transition from widespread volcanism to localized magmatic segments.

The Afar depression is an excellent place to study the evolution of a magmatic system in relation to the ongoing continental-oceanic transition. Here we focus on the Red Sea rift branch activity in Central Afar, where the voluminous and widespread Upper Stratoid Series (hereafter US) are followed by more localized emplacement of the Central Afar Gulf Series (hereafter CAG), marking the transition from wider to localized rifting along the Tendaho-Manda Hararo segment (Fig. 1; Stab et al. 2016; Tortelli et al. 2022). We used a petrologic and geochemical approach based on mineral chemistry and phenocryst texture to investigate the magmatic system evolution during rift localization in Central Afar.

## Geological and volcanological background

The study area is located at the intersection of the northernmost portion of the East African Rift System (i.e., Main Ethiopian Rift, MER) with the Red Sea and Gulf of Aden

rifts in the Afar region to form a rift-rift-rift triple junction (Fig. 1A). In Afar, the transition from continental rifting to oceanic spreading is underway and exposed subaerially (Bastow and Keir 2011; Bastow et al. 2018). The onset of the activity is thought to be related to the arrival of a mantle plume around 45 Ma and the emplacement of the Ethiopian flood basalt volcanic successions, continuing at least until 30 Ma (Ebinger et al. 1993; Rooney 2017; Pik et al. 1999; Hofmann et al. 1997). The rifting between the Arabia, Nubia and Somalian plates started around ~35 Ma in the Gulf of Aden rift, at ~27.5–23.8 Ma in Red Sea rift (Fournier et al. 2010; Bosworth et al. 2005) while seafloor spreading started at ~20 Ma in the Gulf of Aden (Fournier et al. 2010) and at ~4 Ma in the south-central Red Sea (Cochran 1983).

Due to the asynchronous development of multiple rift branches in Afar, the ages of individual Series commonly differ between the rifts (Lahitte et al. 2003b; Le Gall et al. 2015; Rime et al. 2023). However, magmatic, stratigraphic and tectonic studies allow reconstructing the temporal evolution of the Red Sea rift from South Afar (broadly below 11°N) to the formation of the Tendaho-Manda Hararo segment in Central Afar. Volcano-tectonic reconstruction by Wolfenden et al. (2005) suggests that since 16 Ma, the locus of strain in South Afar migrated eastward from the Afar western margin, in agreement with Kalb (1995) indicating a migration of the paleo-depocenter toward Central Afar broadly between 10 and 3 Ma. Starting at ~4.5 Ma the volcanism in Afar is marked by the eruption of the Stratoid Series (Rooney et al. 2023). According to petrological, geophysical and stratigraphic evidence, after the emplacement of the Lower Stratoid Series in South Afar, the locus of strain migrated in Central Afar (Hammond et al. 2011) around 2.6 Ma (Wynn et al. 2008; Tortelli et al. 2022) with the emplacement of the US (Fig. 1 and 2.87–1.18 Ma; Feyissa et al. 2019; Kidane et al. 2003; Lahitte et al. 2003b). Broadly between 1.5 and 0.5 Ma, several silicic central volcanoes were formed and have been interpreted as the precursors of the development of magmatic segments in Central Afar (Barberi and Santacrose 1980; Lahitte et al. 2003a, b). Around 1.1 Ma, rifting progressively localized (Tortelli et al. 2022; Stab et al. 2016), leading to the formation of the Tendaho-Manda Hararo segment in Central Afar and to the emplacement of the CAG (Fig. 1.11–0.49 Ma; Feyissa et al. 2019; Kidane et al. 2003; Lahitte et al. 2003b). The most recent magmatic segment activity in Central Afar, known as Axial Series (<0.65 Ma; Ferguson et al. 2013; Field et al. 2013; Lahitte et al. 2003b; Medynski et al. 2015; Feyissa et al. 2019), can be mainly observed along the Manda Hararo segment (Fig. 1).

The crust in Central Afar ranges between 22 and 30 km thick (Ahmed et al. 2022; Hammond et al. 2011). Crustal scale seismic anisotropy is consistent with the presence of

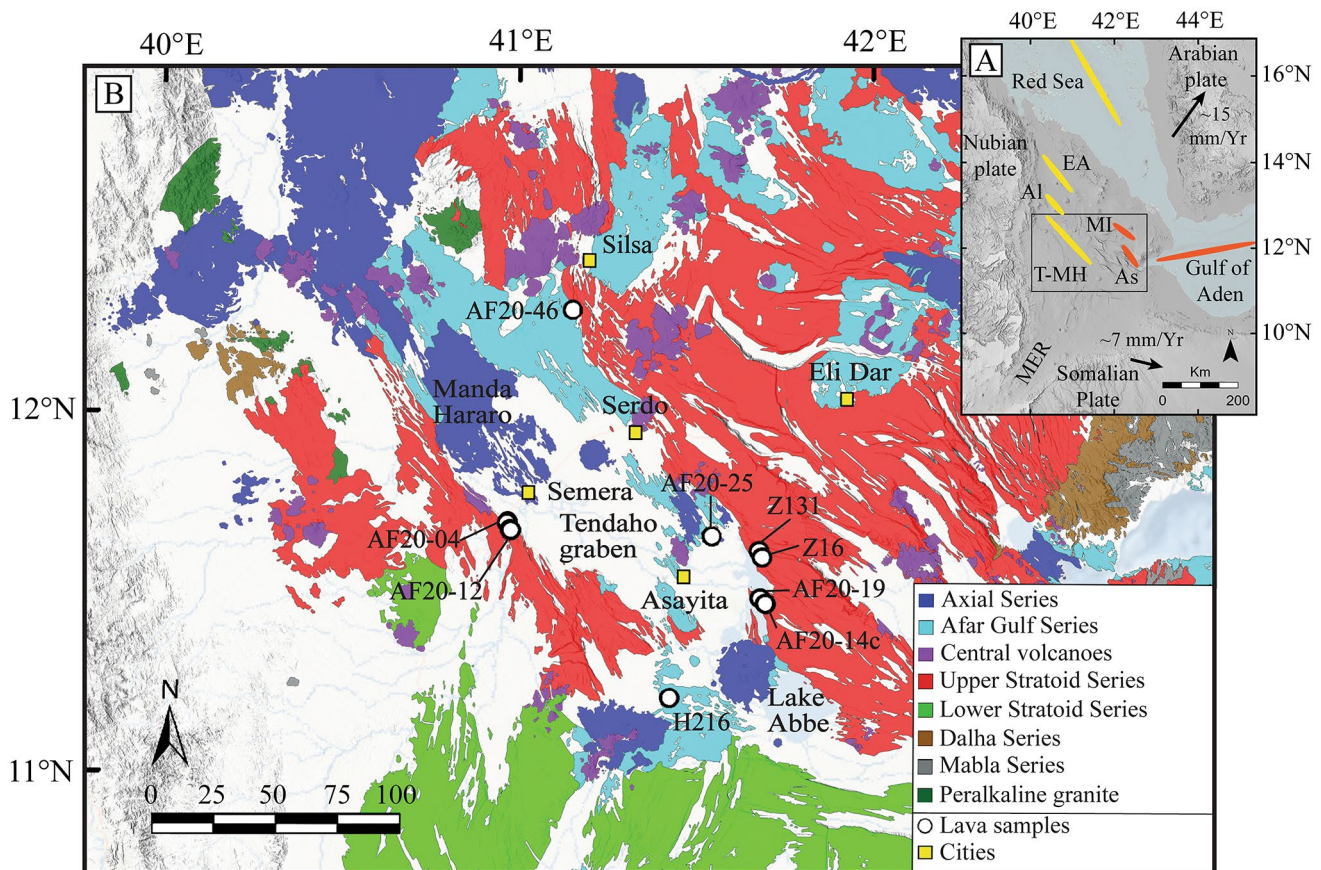


**Fig. 1** (A) Multi-Directional Hillshade map of Afar with Red Sea and Gulf of Aden magmatic segments respectively in yellow and orange. Spreading vector, indicated with arrows, with respect to Nubia fixed plate. The black box encloses the Central Afar represented in picture (B). EA, Erta Ale; AI, Alayta; T-MH, Tendaho-Manda Hararo; As,

Asal; MI, Manda Inakir; MER, Main Ethiopian Rift. (B) Geological map of Central Afar modified from Tortelli et al. (2022), with sampling sites and samples name for the lavas selected for the mineral chemistry study

stacked sills and vertical dikes (Hammond 2014; Chambers et al. 2021). A deep, sill-like region at the Moho level has been suggested using InSAR modeling and magnetotelluric investigation in Afar (Desissa et al. 2013; La Rosa et al. 2024). At the same time, shallow reservoirs have been identified at 5–15 km deep at the Tendaho graben and Manda Hararo magmatic segment (Grandin et al. 2010; Didana et al. 2014). Volatile contents analysis in melt inclusions and modeling of InSAR deformation have been used by Field et al. (2012a) to identify a system of stacked sills from 1 to 5 km below the currently active Dabbahu volcano. In the brittle upper crust, the magma can episodically propagate laterally from one or more magma chambers, feeding dike intrusion or fissural eruptions, such as the 2005–2010 Manda Hararo-Dabbahu rifting event (Wright et al. 2012).

The US are dominated by basaltic lava flow successions, however, primary basalts ( $\text{MgO} > 10$  wt%) are absent and primitive lavas are rarely documented in Central Afar. The erupted magmas are chemically homogeneous and moderately differentiated (Tortelli et al. 2022). The lava flows are

on the order of 10 m thick and generally aphyric, partially preventing the investigation of the magma evolution by mineral chemistry studies. The CAG are instead less voluminous, dominated by meter-thick (up to 2 m) basaltic lava flows slightly more mafic and porphyritic with respect to the Stratoid. The recent study of Tortelli et al. (2022) suggested an evolution through fractional crystallization for both the two Series with considerable differences in the crustal storage and ascent pathways, with the CAG ponding at ~9–16 km and the US directly rising to the surface with no evidence of stationing in the crust.

## Materials and methods

In this work we studied samples of the US and CAG lava flows outcropping in the area of the Tendaho graben in Central Afar (Fig. 1). The samples are from the field campaign conducted in February 2020 and from the collection of the Afar Repository of the University of Pisa (<https://>

repositories.dst.unipi.it/index.php/home-afar). For the present work, six lavas from the February 2020 field campaign and three lavas from the Afar Repository have been selected. The petrography and the whole rock geochemistry of major and trace elements of these products have been previously described in Tortelli et al. (2022) except for two samples that are presented here for the first time (Z16 and Z131; Tab. S1). These two samples have been collected along the Gamarrì escarpment in the Tendaho which is mapped as Upper Stratoid in literature and have an age within the Upper Stratoid age range. The abundance of the phenocrysts has been quantitatively evaluated by comparison with volume % estimation diagrams. Major and trace elements analyses (Tab. S1) were carried out at Activation Laboratories Ltd. (Ontario, Canada) by means of Inductively Coupled Plasma Optical Emission Spectroscopy (ICP-OES) and Inductively Coupled Plasma Mass Spectrometry (ICP-MS).

Polished thin sections were prepared for five US and three CAG mafic lava samples and one US silicic lava samples. These samples were studied by means of Scanning Electron Microscopy-Backscattered Electron Imaging (SEM-BSEI) and energy dispersive X-ray spectroscopy (EDS) microanalysis with the field emission scanning electron microscope FEI Quanta 450 ESEM-FEG provided with a Bruker QUANTAX XFlash Detector 6/10 (Centro per la Integrazione della Strumentazione dell'Università di Pisa, CISUP). Based on the SEM observations, mineral chemistry was then analyzed using a JEOL JXA-8230 superprobe device (joint laboratory of the Dipartimento di Scienze della Terra di Firenze and CNR-IGG). The analytical conditions were 15 kV of accelerating voltage with 20 nA of beam current and 3  $\mu\text{m}$  beam size for olivine, pyroxene, and oxide and 10 nA beam current and 5  $\mu\text{m}$  beam size for plagioclase. The counting time was 15 s on peak and 7 s in the background for major elements (Si, Ti, Al, Fe, Mg, Ca, K) with the exception of Na that is counted for 10 s on peak and 5 s in the background. For minor elements (Mn, Sr, Ba), the counting time was 30–40 s on peak and 15–20 s in the background. The standards used for the calibration are Albite Astimex for Si and Na, Plagioclase Astimex for the Al, Olivine Astimex for the Mg, Diopside Astimex for the Ca, Sanidine Astimex for K, Ilmenite Smithsonian for Ti and Fe, Baryte Astimex for the Ba, Celestite Astimex for the Sr.

In-situ trace element analysis has been performed by LA-ICP-MS on plagioclase phenocrysts of three US and two CAG mafic lava samples previously analyzed by EPMA. The laser ablation-ICP-MS analyses were performed using a PerkinElmer NexION 2000 ICP-MS coupled with a NWR-193 AR-F 193 nm excimer laser, in the Earth Science Department of Pisa, at the CISUP laboratories. The ablation was performed with a spot size of 50–60  $\mu\text{m}$ , fluency of 5 J

$\text{cm}^{-2}$ , 10 Hz repetition rate, warm up time of 20 s, ablation time of 25 s and wash out time of 25 s. Ultrapure He was used as carrier gas. The NIST612 glass reference material was used as external calibration standard, the data reduction was carried out with Iolite v.2.5 (Paton et al. 2011) in quantitative mode and Ca concentrations (analyzed by EPMA) were used as internal standard. The accuracy and precision of the analyses were performed analyzing the NIST610 international standard together with an in-house standard (glass of basalt BE-N). For each session, both the calibrant and the secondary standards were analyzed at the beginning, at the end and every six analyses of the unknown sample to correct for the instrumental drift and improve the quality of the data. Typical precision and accuracy of the NIST610 reference material trace elements are < 15% which improves to < 5–10% for the elements presented in this work (i.e., Sr, Ba and LREE; Table S1).

## Results

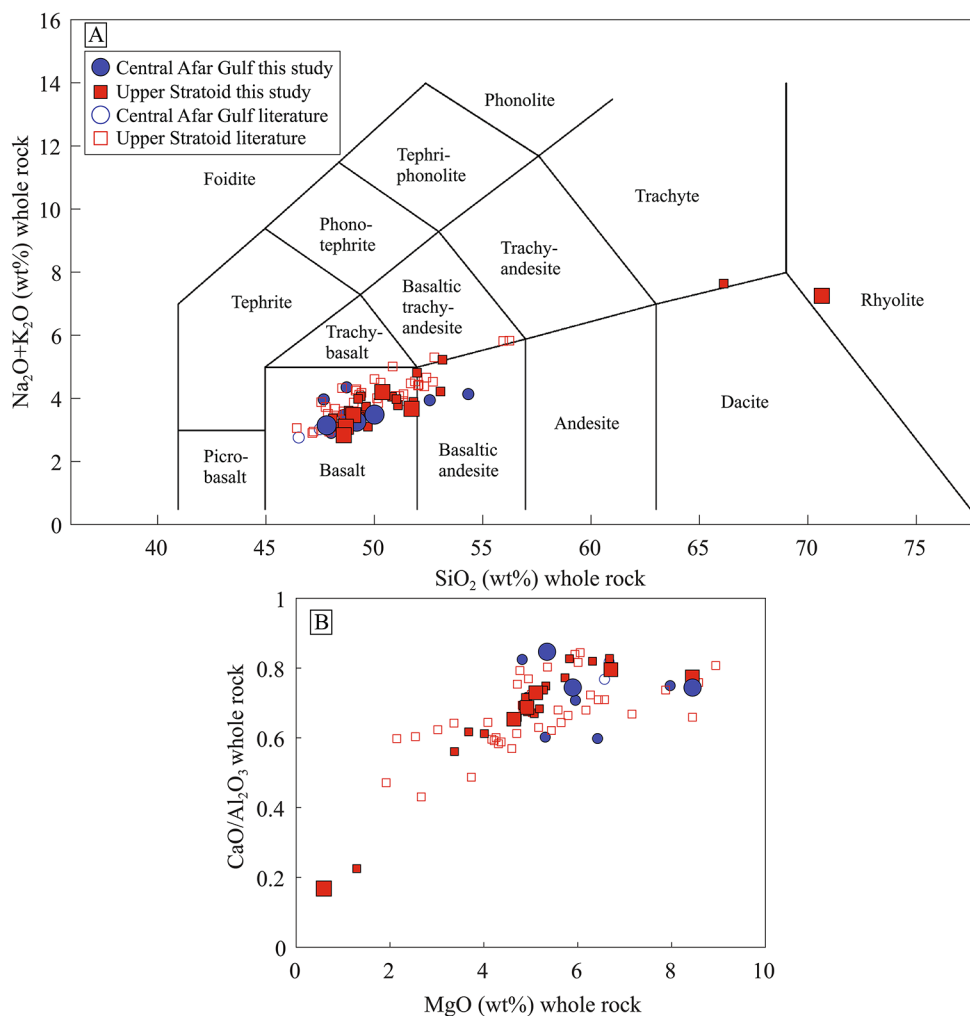
### Rock classification and petrography

The US and CAG Series lavas are mainly basalts and basaltic andesites, with minor evolved products (Fig. 2). Both the Series are subalkaline, with transitional to tholeiitic affinity. The lavas of the US Series are mainly aphyric with rare micro-porphyritic or moderately porphyritic types. Plagioclase is the most abundant phenocryst, while olivine and clinopyroxene are common only in the more primitive lavas. The CAG are micro-porphyritic or porphyritic, rarely aphyric; plagioclase is the most abundant phenocryst phase, but olivine and clinopyroxene phenocrysts are also common (Tortelli et al. 2022; Fig. S1; Tab. S1).

For the microanalytical study we selected five US and three CAG mafic samples from the Tendaho graben, based on the presence of phenocrysts and geochemical characteristics representative of the Series. In particular, for both Series we have selected samples with MgO in the range 4–6 wt% (hereafter low-MgO samples and representing the majority of the erupted lavas; Tortelli et al. 2022) and 6–8.3 MgO wt% (hereafter high-MgO samples). Furthermore, the only US silicic lava flow, collected within the US lava successions in the Tendaho graben area, has been analyzed (rhyolite sample AF20-14c; Figs. 1 and 2).

The US high-MgO samples are presented here for the first time and represent the most primitive lavas (up to 8.3 MgO wt%) erupted during the US phase (Fig. 2). The high-MgO samples are moderately porphyritic (10–15% vol.) with olivine and clinopyroxene phenocrysts more abundant than plagioclase (Fig. S1A; Tab S1). The US low-MgO range from nearly aphyric to plagioclase-dominated

**Fig. 2** (A) TAS (Total Alkali vs. Silica, wt%) classification diagram for US and CAG lavas. Data recalculated to 100% on a water-free basis. Total iron as  $\text{FeO}_{\text{tot}} = \text{FeO} + \text{Fe}_2\text{O}_3 \cdot 0.8998$ . (B)  $\text{CaO}/\text{Al}_2\text{O}_3$  vs.  $\text{MgO}$  diagrams for US and CAG lavas. Literature data are from Tortelli et al. (2022), Feyissa et al. (2019) and Barberi and Santacroce (1980). All analyses are reported in Tab. S1



porphyritic samples (up to 35% vol.) with rare clinopyroxene and olivine (Fig. S1A; Tab. S1). The US rhyolitic sample is moderately porphyritic (15% vol.) and phenocrysts are mainly feldspar and clinopyroxene (Fig. S1B; Tab. S1). The CAG high-MgO sample has an ophitic texture dominated by clinopyroxene and olivine with minor plagioclase (10% vol.). The CAG low-MgO are porphyritic (up to 20% vol.), plagioclase-dominated but showing an increase in size and abundance of clinopyroxene and olivine with respect to the US low-MgO samples (Fig. S1C; Tab. S1). Two different Fe-Ti oxides (Ti-magnetite and ilmenite) have been observed in all the samples, while apatite has been observed only in the US rhyolitic sample. For both Series, the groundmass is composed of plagioclase, clinopyroxene, Fe-Ti oxides and, occasionally, olivine. Furthermore, both the CAG low-MgO samples show textural heterogeneity consisting in different crystal abundance and groundmass grain size (Fig. S1C).

## Mineral chemistry

In this section we present the mineral chemistry results of plagioclase and clinopyroxene, for high- and low-MgO samples of the two Series (Figs. 3 and 4; Fig. S2; Tab. S1) and the plagioclase analysis of the US rhyolitic sample (Fig. 3; Tab. S1). The mineral chemistry results of olivine and Fe-Ti oxides are described in the Supplementary Text file.

### Plagioclase

The plagioclase covers an overall similar compositional range in the two Series, with phenocryst composition from bytownite to andesine ( $\text{An}_{24-88}$  for the US and  $\text{An}_{27-85}$  for the CAG) (Fig. 3A, B), and a bimodal distribution of the core composition (modes  $\text{An}_{67}$  and  $\text{An}_{83}$  for the US and modes  $\text{An}_{71}$  and  $\text{An}_{78}$  for the CAG, Fig. 3C, D). The bimodality in the plagioclase core composition corresponds to the low-MgO and high-MgO rock groups for both Series (Fig. 3E, F, G, H).

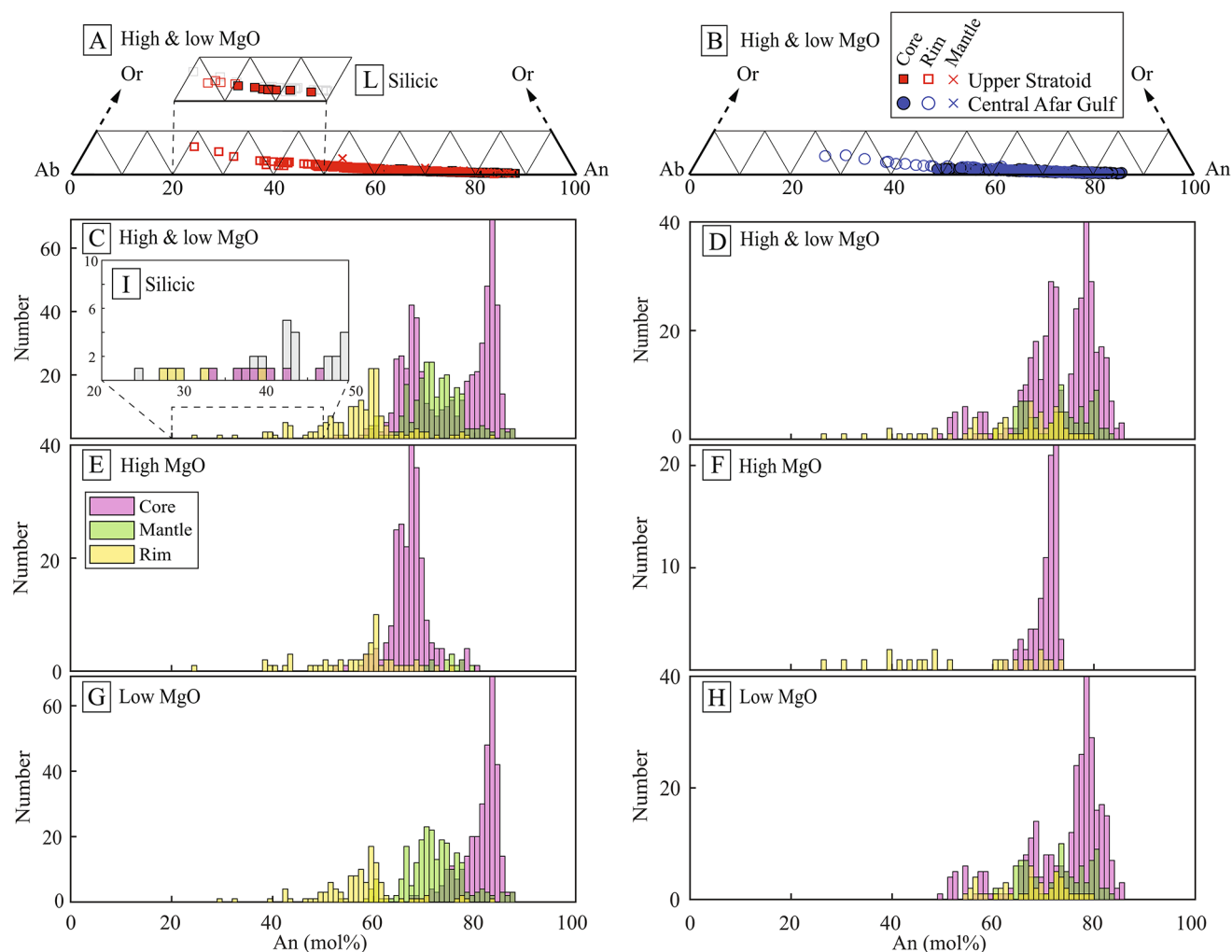


**Fig. 3** (A, B) Feldspar (An-Ab-Or) classification diagrams of US (A) and CAG (B) high- and low-MgO samples. (C-H) Feldspar histogram (An) for core, mantle and rim analysis of US and CAG. For each Series the samples are plotted all together (C, D) and divided in high- and low-MgO samples (E-H). US high- and low-MgO (C), high-MgO

(E) and low-MgO (G) samples are on the left side. CAG high- and low-MgO (D), high-MgO (F) and low-MgO (H) samples are on the right side. (L, I) Feldspar (An-Ab-Or) classification diagrams (L) and histogram (An) for core and rim (I) of the US rhyolitic sample (inset in A and C). In gray are reported the US high- and low-MgO analysis

Regarding the US high-MgO samples, plagioclase phenocrysts are mainly normally zoned or unzoned, with core composition corresponding to the lower An group of the US core analyses (Fig. 3C; range  $An_{53-80}$  and mode  $An_{67}$ ) and similar or lower An for the rim (range  $An_{24-76}$  and mode  $An_{60}$ ) (Fig. 3E). However, a few plagioclase show an intermediate portion (i.e., mantle) between core and rim, showing a more complex, oscillatory or reverse, zoning ( $An_{75-80}$  in Fig. 3E) followed by a lower An rim. In the US low-MgO samples the plagioclase crystals are normally zoned, with core composition corresponding to the higher An group of the US core analyses (Fig. 3C; range  $An_{54-88}$  and mode  $An_{83}$ ) and a compositional gap with the lower An rim (range  $An_{24-84}$  and mode  $An_{59}$ ). This gap between core and rim is partially covered by the composition of the mantle (range  $An_{53-87}$  and mode  $An_{71}$ ) (Fig. 3G). The plagioclase

phenocrysts of the US rhyolitic sample range from oligoclase to andesine ( $An_{28-47}$ ) and are all normally zoned (Fig. 3I, L).

Regarding the CAG, the high-MgO samples have normally zoned or unzoned plagioclase, with core composition corresponding to the lower An group of the CAG core analyses (Fig. 3D; range  $An_{63-74}$  and mode  $An_{72}$ ) and similar or lower An for the rim (range  $An_{27-73}$ ) (Fig. 3F). In the CAG low-MgO samples plagioclase phenocrysts with normal and reverse zoning coexist, with the more represented core composition corresponding to the higher An group of the CAG core analyses (Fig. 3D;  $An_{78}$ ). In these samples the plagioclase core, mantle and rim compositions broadly overlap, with the cores having a major mode at  $An_{78}$  and two minor modes at  $An_{54}$  and  $An_{68}$  while mantle and rim composition range at  $An_{60-83}$  and  $An_{54-80}$  respectively (Fig. 3H).

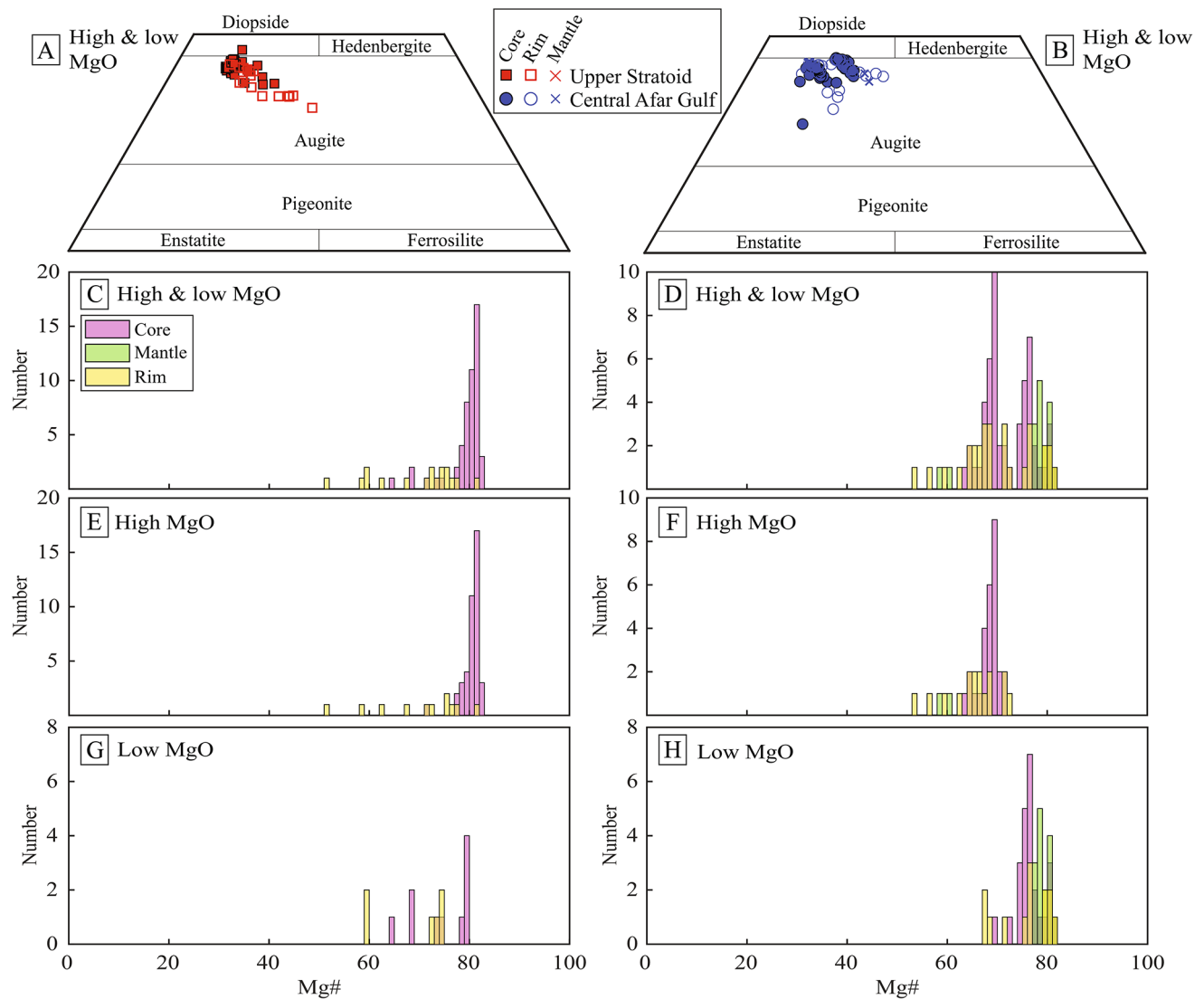


**Fig. 4** (A, B) Clinopyroxene (En-Fs-Hd-Di) classification diagrams of US (A) and CAG (B) high- and low-MgO samples. (C-H) Clinopyroxene histogram ( $Mg\# = (Mg/[Mg + Fe] \times 100)$ ) for core, mantle and rim analysis of US and CAG. For each Series the samples are plotted all

together (C, D) and divided in high- and low-MgO samples (E-H). US high- and low-MgO (C), high-MgO (E) and low-MgO (G) samples are on the left side. CAG high- and low-MgO (D), high-MgO (F) and low-MgO (H) samples are on the right side

## Clinopyroxene

All the clinopyroxenes of both series have broadly similar augitic composition in the pyroxene quadrilateral Di-Hd-En-Fs, close to the diopside field (Fig. 4A, B). In detail, the CAG high-MgO sample shows a small but significant sub-trend shifted toward the hedenbergite field (Fig. 4B). The two series have indeed a similar compositional range (range  $Mg\#_{52-82}$  and  $Mg\#_{54-81}$  for the US and CAG respectively;  $Mg\# = (Mg/[Mg + Fe] \times 100)$ ) but depict a unimodal distribution for the US core composition (mode  $Mg\#_{81}$ ) and a bimodal distribution for the CAG core composition (mode  $Mg\#_{69}$  and  $Mg\#_{76}$ ) (Fig. 4C, D). Similarly to the plagioclase,

the bimodality of the CAG core composition corresponds to the low-MgO and high-MgO rock groups (Fig. 4E, F, G, H).

Regarding the US, the high-MgO samples have normally zoned clinopyroxene with high  $Mg\#$  values in the core (range  $Mg\#_{71-82}$  and mode  $Mg\#_{81}$ ) and lower  $Mg\#$  for the rim (range  $Mg\#_{52-81}$ ) (Fig. 4E). The US low-MgO samples have few and unzoned clinopyroxene with variable  $Mg\#$  for the core (range  $Mg\#_{65-80}$ ) and similar or lower  $Mg\#$  for the rim (range  $Mg\#_{59-75}$ ) (Fig. 4G).

Regarding the CAG, the high-MgO samples have normally zoned or unzoned clinopyroxene with core composition corresponding to the lower  $Mg\#$  mode (range  $Mg\#_{64-72}$  and mode  $Mg\#_{69}$ ) and overlapping or slightly lower  $Mg\#$  for the rim (range  $Mg\#_{54-73}$ ) (Fig. 4F). The CAG low-MgO

samples have normally and, in some cases, reversely zoned clinopyroxene with core composition corresponding to the higher Mg# mode (range Mg#<sub>69–81</sub> and mode Mg#<sub>76</sub>). Slightly higher Mg# values (up to 82) are recorded in many mantle zones and some rims (Fig. 4H).

### Phenocrysts textures and chemical zoning

In this section, we describe the texture and chemical zoning of US plagioclase and CAG plagioclase and clinopyroxene.

In particular we focus on An-TiO<sub>2</sub> and Mg#-Cr<sub>2</sub>O<sub>3</sub> variations respectively for plagioclase and clinopyroxene phenocrysts (Figs. 5 and 6; Fig. S3). Regarding the trace element we focus on the Sr-Ba variations for plagioclase phenocrysts (Fig. 7A; Fig. S4).

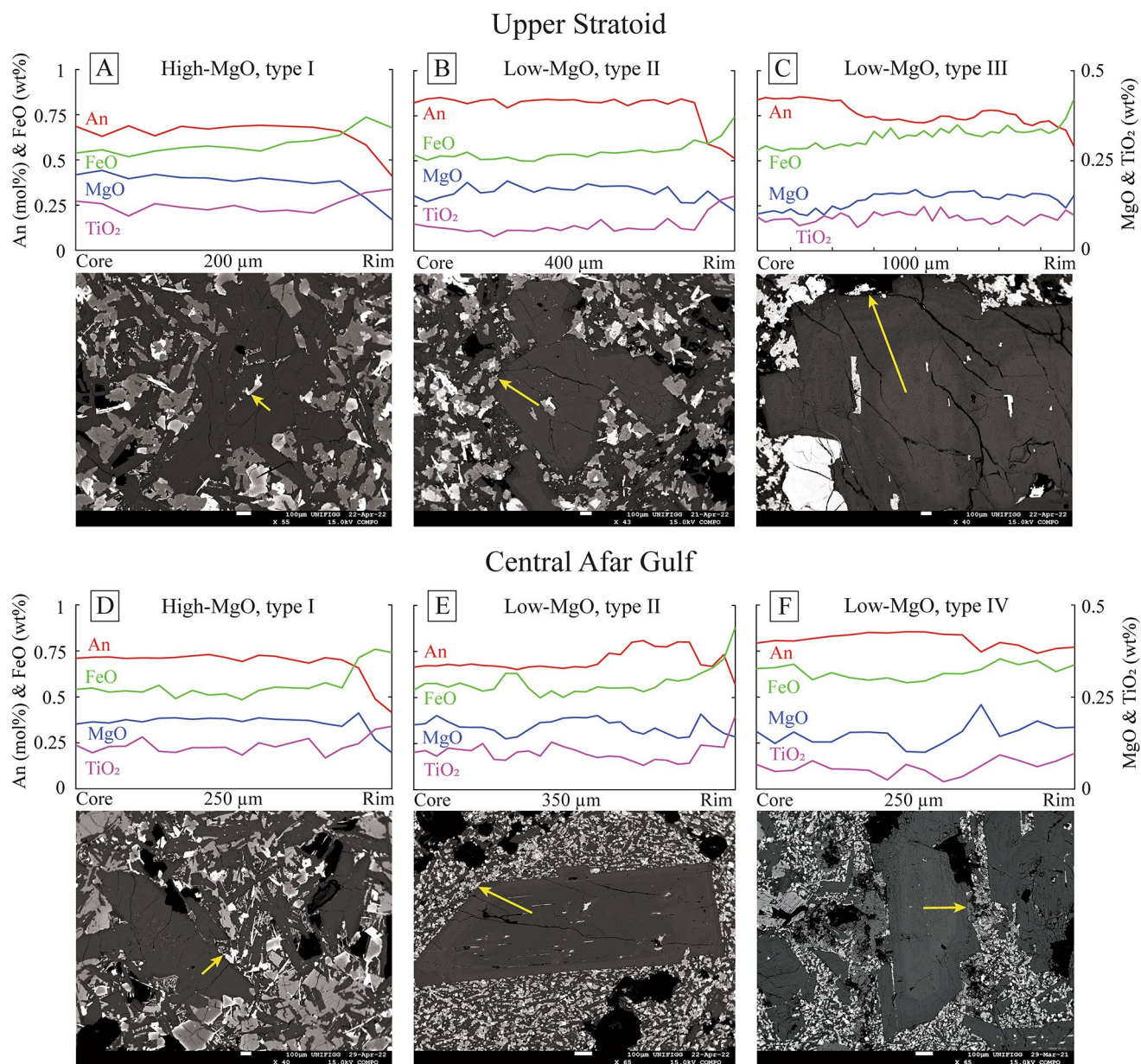


**Fig. 5** (A–F) Plagioclase compositional profiles of An, FeO<sub>tot</sub>, TiO<sub>2</sub> and MgO concentration with relative backscatter electron (BSE) images, representative of the different plagioclase types for US (A–C) and CAG (D–F) samples. (A) US high-MgO sample, (B, C) US low-MgO samples, (D) CAG high-MgO sample, (E, F) CAG low-MgO

samples. The location of the analysis profile is indicated with a yellow arrow in each BSE image. Each profile is titled with the low- or high-MgO representative group and the crystal type (description in text). All plagioclase profiles and relative BSE images are in Fig. S3



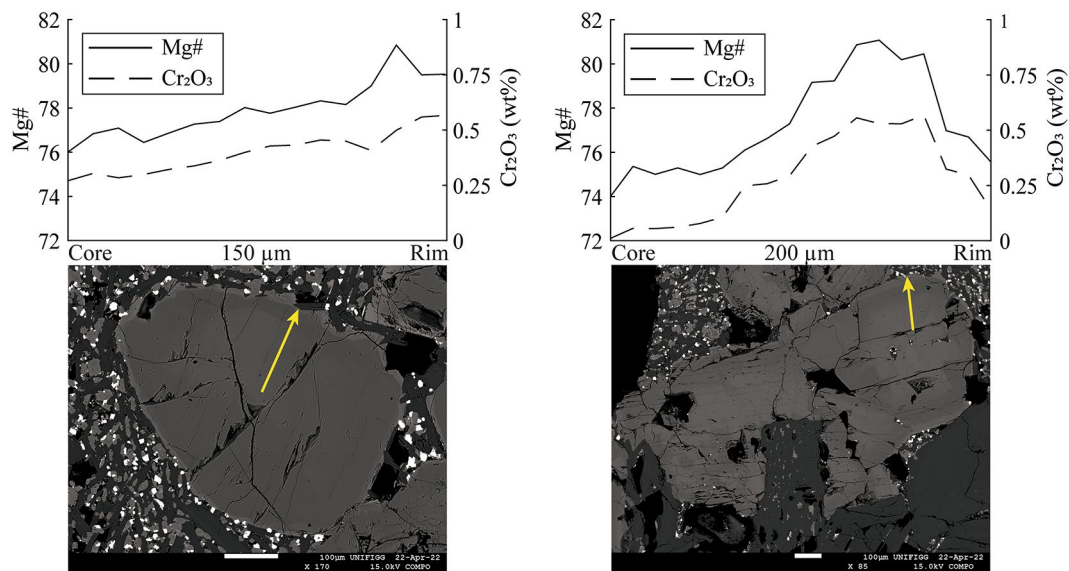


**Fig. 6** Clinopyroxene compositional profiles of Mg# content ( $Mg\# = (Mg/(Mg + Fe_{2+}) \times 100)$ ) and  $Cr_2O_3$  concentration with relative BSE images for CAG low-MgO samples. The location of the analysis profile is indicated with a yellow arrow in each BSE image

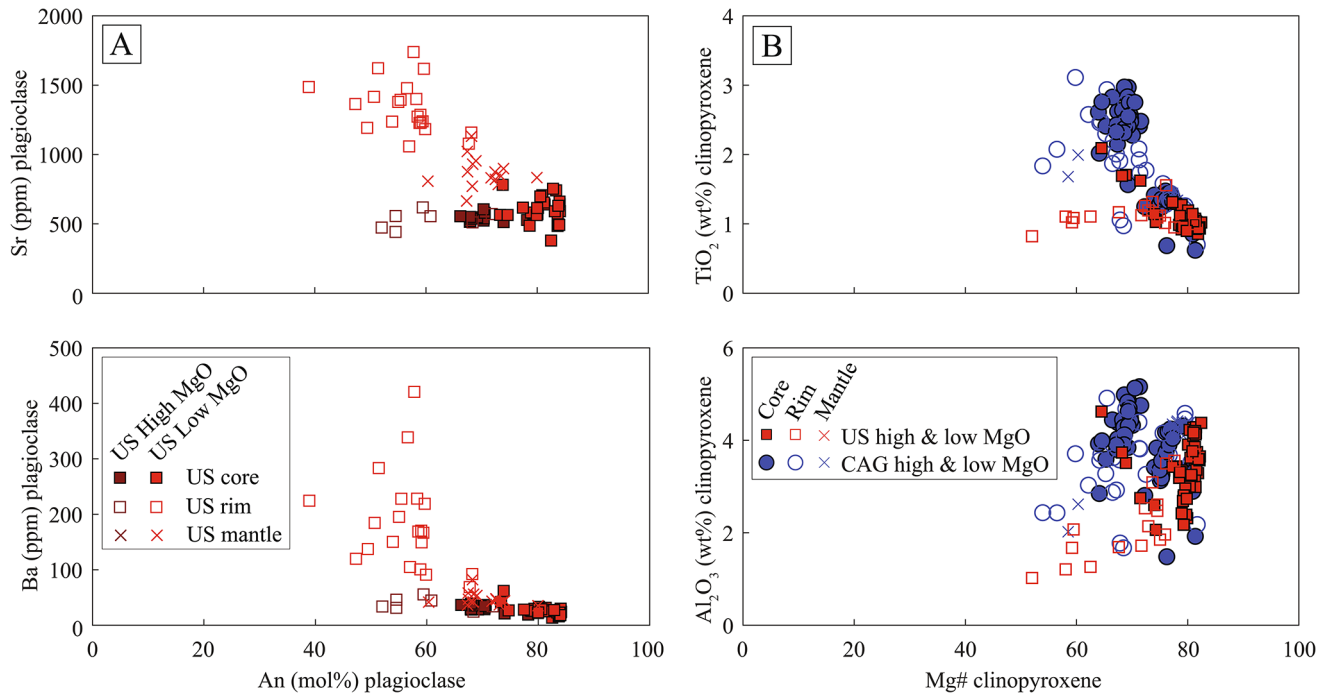


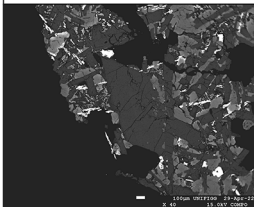
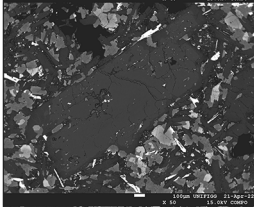
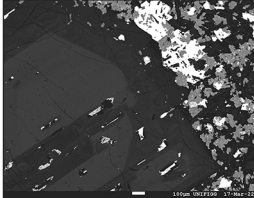
**Fig. 7** (A) Variation of Sr, Ba and Eu trace element concentrations versus An contents of US and CAG plagioclase. All trace element variation diagrams are in Fig. S4 and the LA-ICP-MS data are listed in Tab. S1. (B) Variation of  $TiO_2$  and  $Al_2O_3$  versus magnesium number ( $Mg\#$

$= (Mg/(Mg + Fe_{2+}) \times 100)$  showing the differences between US and CAG and the CAG internal variability. All variation diagrams are in Fig. S2 and the EPMA data are listed in Tab. S1

**Upper Stratoid**

We identify one main plagioclase typology for the US high-MgO samples and two for the US low-MgO samples (Fig. 8; Fig. S3A, B).

The prevalent plagioclase type in US high-MgO samples (Type I in Fig. 5A and Fig. S3A) is normally zoned, with a homogeneous core with average  $An_{67}$  and no or very thin rims averaging at  $An_{43}$ . Accordingly, high  $TiO_2$  content, slightly increasing from core (mean 0.12 wt%) to rim (mean 0.15 wt%), has been observed. Regarding trace elements, Sr

Upper Stratoid	Name	Petrographic observations	Major and trace element mineral chemistry		
			Core	Mantle	Rim
	High-MgO Type I	<ul style="list-style-type: none"> <li>• Normally zoned</li> <li>• Homogenous cores</li> <li>• Thin rims</li> </ul>	An 67 - TiO <sub>2</sub> 0.12 Sr 553 - Ba 33	-	An 43 - TiO <sub>2</sub> 0.15 Sr 531 - Ba 39
	Low-MgO Type II	<ul style="list-style-type: none"> <li>• Normally zoned</li> <li>• Homogeneous and resorbed cores, sometimes sieved</li> <li>• Thin rims</li> </ul>	An 82 - TiO <sub>2</sub> 0.07 Sr 580 - Ba 28	-	An 53 - TiO <sub>2</sub> 0.15 Sr 1378 - Ba 211
	Low-MgO Type III	<ul style="list-style-type: none"> <li>• Normally zoned</li> <li>• Homogeneous and resorbed cores, sometimes sieved</li> <li>• Sometimes oscillatory mantles</li> </ul>	An 82 - TiO <sub>2</sub> 0.07 Sr 641 - Ba 25	An 72 - TiO <sub>2</sub> 0.10 Sr 870 - Ba 47	An 57 - TiO <sub>2</sub> 0.13 Sr 1202 - Ba 95

**Fig. 8** Summary of textural and compositional characteristics of the different plagioclase types for the US high- and low-MgO samples. An and TiO<sub>2</sub> are expressed in mol% and wt% respectively while Sr and Ba concentrations in ppm. See text for discussion

has a constant trend from core (mean 553 ppm) to rim (mean 531 ppm) while Ba shows a slight increase from core (mean 33 ppm) to rim (mean 39 ppm) (Fig. 7). Few plagioclase (crystal 1 and 10.1 in Fig. S3A) have portions (i.e., mantle and core) enriched in An and depleted in TiO<sub>2</sub>.

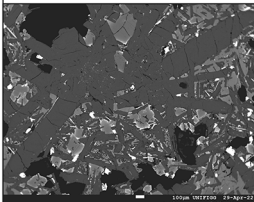
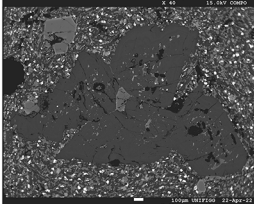
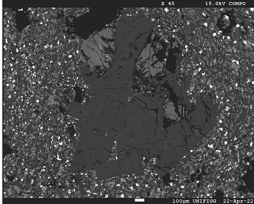
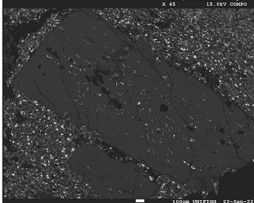
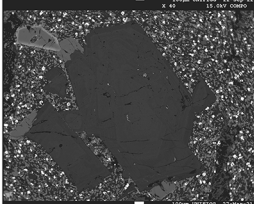
Two main types have been observed for the US low-MgO samples: Type II) homogeneous and resorbed cores, sometimes sieved, with high An (mean An<sub>82</sub>) and low TiO<sub>2</sub> (mean 0.07 wt%). The rims are thin and marked by an abrupt decrease in An (mean An<sub>53</sub>) and increase in TiO<sub>2</sub> (mean 0.15 wt%) (Fig. 5B; Type II in Fig. S3B); Type III) homogeneous resorbed cores, sometimes sieved, with high An (mean An<sub>82</sub>) and low TiO<sub>2</sub> (mean 0.07 wt%) mostly show an abrupt normal zonation to an oscillatory or homogeneous mantle, averaging An<sub>72</sub> and showing an increase in TiO<sub>2</sub> (mean 0.10 wt%) (Fig. 5C; Type III in Fig. S3B). At times a core to rim gradual variation, from light- to dark-gray shade, is observed in BSE images, confirmed by the An and TiO<sub>2</sub> contents (Type III in Fig. S3B). The crystals show homogenous rims, with a decrease in An (mean An<sub>57</sub>) and increase in TiO<sub>2</sub> (mean 0.13 wt%) with respect to the mantle. Both the US low-MgO samples have an increase in Sr and Ba from core (mean Sr 602 ppm and Ba 27 ppm) to mantle (mean Sr 870 ppm and Ba 47 ppm) to rim (mean Sr 1336 ppm and Ba 183 ppm) (Fig. 7).

### Central Afar Gulf

We identify one main plagioclase typology for the CAG high-MgO samples while four have been identified for the CAG low-MgO samples (Fig. 9; Fig. S3C, D).

The plagioclase phenocrysts of high-MgO CAG samples, similarly to those in the high-MgO samples of US, have homogeneous cores with constant and relatively low An, averaging An<sub>70</sub>, and high TiO<sub>2</sub> (0.11 wt%); they have no or very thin rims, showing a decrease in An (mean An<sub>47</sub>) and increase in TiO<sub>2</sub> (0.15 wt%) with respect to the core (Fig. 5D; Type I in Fig. S3C).

The low-MgO CAG plagioclase, on the contrary, show more overall complexity compared to the US, and four different types of plagioclase have been recognised (Fig. 5E, F; Fig. S3D): Type II) mainly sieved and resorbed cores with variable An (range An<sub>55-82</sub>) and low TiO<sub>2</sub> (mean 0.10 wt%), with complex mantles showing oscillatory and/or reverse zoning with An averaging An<sub>75</sub> and overall similar or lower TiO<sub>2</sub> (mean 0.09 wt%). The rims show a decrease in An (mean An<sub>65</sub>) and increase in TiO<sub>2</sub> (mean 0.15 wt%) (Fig. 5E; Type II in Fig. S3D). Type III) Homogeneous or slightly oscillatory cores with high An (mean An<sub>74</sub>) and low TiO<sub>2</sub> (mean 0.09 wt%). The mantles show an abrupt decrease in An (mean An<sub>66</sub>) and a small increase in TiO<sub>2</sub> (mean 0.11 wt%), sometimes having a small reverse zoned portion toward the rims with an increase in An and decrease in TiO<sub>2</sub>. No, or thin normally zoned rims (mean An<sub>60</sub> and

Central Afar Gulf	Name	Petrographic observations	Major and trace element mineral chemistry		
			Core	Mantle	Rim
	High-MgO Type I	<ul style="list-style-type: none"> <li>• Normally zoned</li> <li>• Homogenous cores</li> <li>• Thin rims</li> </ul>	An 70 - TiO <sub>2</sub> 0.11	-	An 47 - TiO <sub>2</sub> 0.15
	Low-MgO Type II	<ul style="list-style-type: none"> <li>• Complex zoning</li> <li>• Sieved and resorbed cores</li> </ul>	An 70 - TiO <sub>2</sub> 0.10 Sr 512 - Ba 32	An 75 - TiO <sub>2</sub> 0.09 Sr 488 - Ba 26	An 65 - TiO <sub>2</sub> 0.15 Sr 535 - Ba 50
	Low-MgO Type III	<ul style="list-style-type: none"> <li>• Complex zoning</li> <li>• Homogeneous or slightly oscillatory cores</li> </ul>	An 78 - TiO <sub>2</sub> 0.09 Sr 514 - Ba 33	An 72 - TiO <sub>2</sub> 0.10 Sr 529 - Ba 46	An 60 - TiO <sub>2</sub> 0.21 Sr 548 - Ba 42
	Low-MgO Type IV	<ul style="list-style-type: none"> <li>• Normally zoned</li> <li>• Homogeneous or lightly oscillating resorbed cores, reversely zoned</li> </ul>	An 79 - TiO <sub>2</sub> 0.07 Sr 494 - Ba 25	-	An 72 - TiO <sub>2</sub> 0.09 Sr 450 - Ba 26
	Low-MgO Type V	<ul style="list-style-type: none"> <li>• Normally zoned</li> <li>• Homogeneous or lightly oscillating resorbed cores, normally zoned</li> </ul>	An 77 - TiO <sub>2</sub> 0.07 Sr 568 - Ba 24	-	An 66 - TiO <sub>2</sub> 0.10 Sr 563 - Ba 33

**Fig. 9** Summary of textural and compositional characteristics of the different plagioclase types for the CAG high- and low-MgO samples. An and TiO<sub>2</sub> are expressed in mol% and wt% respectively while Sr and Ba concentrations in ppm. See text for discussion

TiO<sub>2</sub> 0.21 wt%) have been observed (Type III in Fig. S3D). Type IV) Homogeneous or lightly oscillating resorbed cores (one sieved) with constant or gradual and small (one with a more marked step) increase in An (range An<sub>68–85</sub>) and slightly increasing or constant TiO<sub>2</sub> (mean 0.07 wt%) (Fig. 5F; Type IV in Fig. S3D). No rims or normally zoned rims (mean An<sub>72</sub> and TiO<sub>2</sub> 0.09 wt%) have been observed. Type V) Homogeneous or slightly oscillatory, resorbed cores with a gradual and small decrease in An (range An<sub>65–83</sub>) and slightly increasing or constant TiO<sub>2</sub> (mean 0.07 wt%) (Type V in Fig. S3D). No rims or normally zoned rims (mean An<sub>66</sub> and TiO<sub>2</sub> 0.10 wt%) have been observed. Regarding trace elements for all the low-MgO CAG typologies, Sr have a constant trend (mean core 507 ppm, mantle 507 ppm and

rim 505 ppm) while Ba show a slight increase from core and mantle (mean 28 ppm) to rim (37 ppm) (Fig. 7).

Although this study is mainly focused on the plagioclase as it is the most abundant phenocryst phase (particularly for the US), for the CAG we also carried out profile analysis for the clinopyroxene, which is a relatively common phenocryst in low-MgO CAG, also. The two low-MgO CAG clinopyroxene analyzed shows oscillatory and reverse zoning with rim and mantle reaching higher Mg# and Cr<sub>2</sub>O<sub>3</sub> (respectively up to 81 and 0.57 wt%) with respect to the cores (up to Mg# 77 and Cr<sub>2</sub>O<sub>3</sub> 0.32 wt%; Fig. 6).

## Mineral-melt equilibrium and geothermobarometry

Geothermobarometry estimations have been obtained using the phenocryst compositions of plagioclase and clinopyroxene in both US and CAG Series. We used the plagioclase geothermobarometer of Putirka (2008) to calculate the pressure and temperature of crystallization. The clinopyroxene pressure and temperature of crystallization has been calculated using the methods of Neave and Putirka (2017) and Putirka (2008) respectively (Tab. S1). We used the whole rock analysis as the melt composition. The equilibrium was checked based on the plagioclase-clinopyroxene-liquid distribution coefficient of Putirka (2008) (see [Supplementary Text](#)) and the water concentration input set at 0.5 wt% according to literature evidence (Field et al. 2012b, 2013; Tortelli et al. 2022). We estimated the storage conditions of the magma based on phenocryst core and mantle analyses in equilibrium with the host rock. The corresponding depths have been derived assuming a 270 bar/km geobaric gradient (Best 2013).

Regarding the US high- and low-MgO samples, both clinopyroxene and plagioclase indicate pressure of mainly 2–5 kbar and temperature ranging from 1125 to 1200 °C (Fig. 10). Only a few plagioclase crystals belonging to one low-MgO sample with low An ( $An_{69-76}$ ) core crystallized at very shallow depth (equilibrium at <1 km of depth, Fig. 10). For the US rhyolitic sample, the plagioclase in equilibrium with the host rock indicates broadly 2–4 kbar and temperature ranging between 960 °C and 980 °C (Fig. 10). Similarly to the US, the CAG high- and low-MgO samples clinopyroxene and plagioclase indicate mainly 2–5 kbar and temperature ranging from 1145 to 1175 °C (Fig. 10; [Supplementary Text](#) for a detailed description).

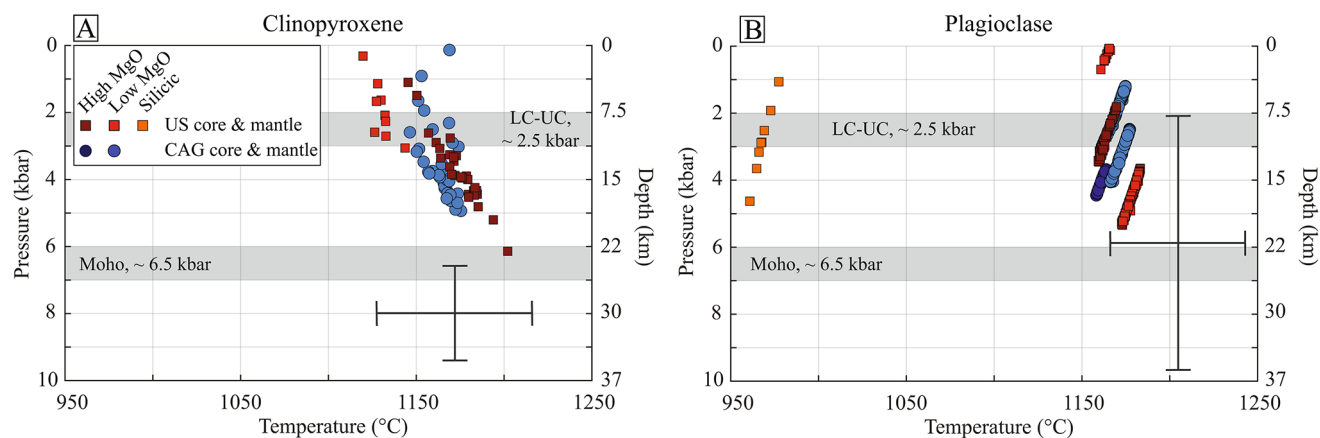


**Fig. 10** (A) Pressure and temperature estimates from clinopyroxene-melt pairs calculated with Neave and Putirka (2017; Eq. 1) and Putirka (2008; Eq. 33). The standard errors of estimate (SEE) for the clinopyroxene-melt thermobarometer are  $\pm 45$  °C and  $\pm 1.2$  kbar and the error bars are shown. (B) Pressure and temperature estimates from plagioclase-melt pairs calculated with Putirka (2008; Eq. 24a and 25a). SEE for the plagioclase-melt thermobarometer are  $\pm 36$  °C and  $\pm 3.8$  kbar and the error bars are shown. The depth of the moho and of the lower-upper crust limit are from Hammond et al. (2011)

Given the large error associated with these geothermobarometers, and in particular with those derived from plagioclase (Fig. 10; Putirka 2008; Neave and Putirka 2017; Wieser et al. 2023), in the discussion we use only the clinopyroxene barometer to estimate the depth of the magmatic system. Most of the estimates for both Series focus at or below the upper-lower crust transition, broadly at ~10–18 km ( $\pm 4$  km), reasonably excluding a very shallow (upper crust) magmatic system.

## Discussion

### US magmatic evolution: insight from whole rock geochemistry

To constrain magmatic differentiation, we calculated the fractional crystallization liquid line of descent (LLD) and the resulting mineral phase compositions using Rhyolite-MELTS (Gualda et al. 2012) by AlphaMELTS software (Smith and Asimow 2005). According to AlphaMELTS best fit conditions we then used Magma Chamber Simulator software (MCS; Bohron et al. 2020; Heinonen et al. 2020) to model Sr and Ba trace elements. We performed the modeling only for the US lavas due to the large number of data available for constraining the model.

We used as the starting composition the most primitive lava analyzed in this work (Z16, MgO wt% 8.3) and modeled liquid evolution for given values of P, T,  $fO_2$  and  $H_2O$  wt%, by free-energy minimization at each  $\Delta T$  step. Each run starts at the liquidus temperature (calculated by MELTS) and, based on the clinopyroxene barometric estimates, we used 4 kbar as the starting depth. According to literature estimation of Afar magmas, we used the water concentration

of 0.5 and 1 wt% (Field et al. 2012b, 2013; Tortelli et al. 2022) and  $fO_2$  of QFM -0.5 and QFM -1 (Bizouard et al. 1980; de Moor et al. 2013; Tortelli et al. 2022). For each initial P-T-H<sub>2</sub>O- $fO_2$  combination, we let the magma undergo fractional crystallization at the pressure of 4 kbar, or start decompressing at different degrees of evolution and at different  $\Delta P$  to evaluate the modeled behaviour at shallower depth (Fig. S5). Our modeling best fits the drop in Al<sub>2</sub>O<sub>3</sub> due to *plagioclase-in* at MgO 5.8–6.7 wt% and in FeO<sub>t</sub> and TiO<sub>2</sub> due to *spinel-in* at MgO 4.5–5 wt% given QFM -0.5, H<sub>2</sub>O 0.5 wt%,  $\Delta P$  30 bar/C° and P 4 kbar as starting conditions (Fig. 11; Fig. S5). Furthermore, the plagioclase-in composition obtained by the MELTS best fit models (An<sub>71–74</sub>) is in excellent agreement with the core compositions of the analyzed plagioclase in equilibrium with Z16 whole rock (An<sub>69–73</sub>). The scatter in Al<sub>2</sub>O<sub>3</sub> observed at 5–6 wt% MgO is well fitted by varying the depth of crystallization (i.e., the initial MgO wt% content of the ascending magma; Fig. 11), while the variation in FeO<sub>tot</sub>, TiO<sub>2</sub> and CaO requires slight variation in H<sub>2</sub>O and  $fO_2$  (Fig. S5). The variation of  $\Delta P$  has an effect similar to varying the initial MgO wt% content of the ascending magma. Indeed a slow rise (i.e., low  $\Delta P$ )

will let the magma fractionate deeper for a longer time with respect to a rapid rise.

Starting from the most mafic samples (Z16), the MCS modeling has been performed using AlphaMELTS best fit conditions of QFM -0.5, H<sub>2</sub>O 0.5 wt% and, in order to account for the variation in depth of crystallization, P of 2, 3 and 4 kbar. The K<sub>d</sub> of Sr and Ba has been calculated using Dohmen and Blundy (2014) according to the most mafic and silicic plagioclase composition calculated by AlphaMELTS (respectively Sr 1.78, Ba 0.21 and Sr 6.15, Ba 0.43). During the modeling the K<sub>d</sub> varied between the mafic and silicic end-member according to MCS calculated temperature. In agreement with the major elements modeling, Sr and Ba analysis are very well fitted by a fractional crystallization trend, up to the most evolved composition (Fig. 12). Only two samples have a remarkably high concentration of respectively Sr and Ba compared to the modeled trend.

### US and CAG magmatic evolution: insights from mineral chemical zoning

In this section we use major and trace elements measured in US and CAG plagioclase (i.e., An, TiO<sub>2</sub>, Sr, Ba) and in CAG

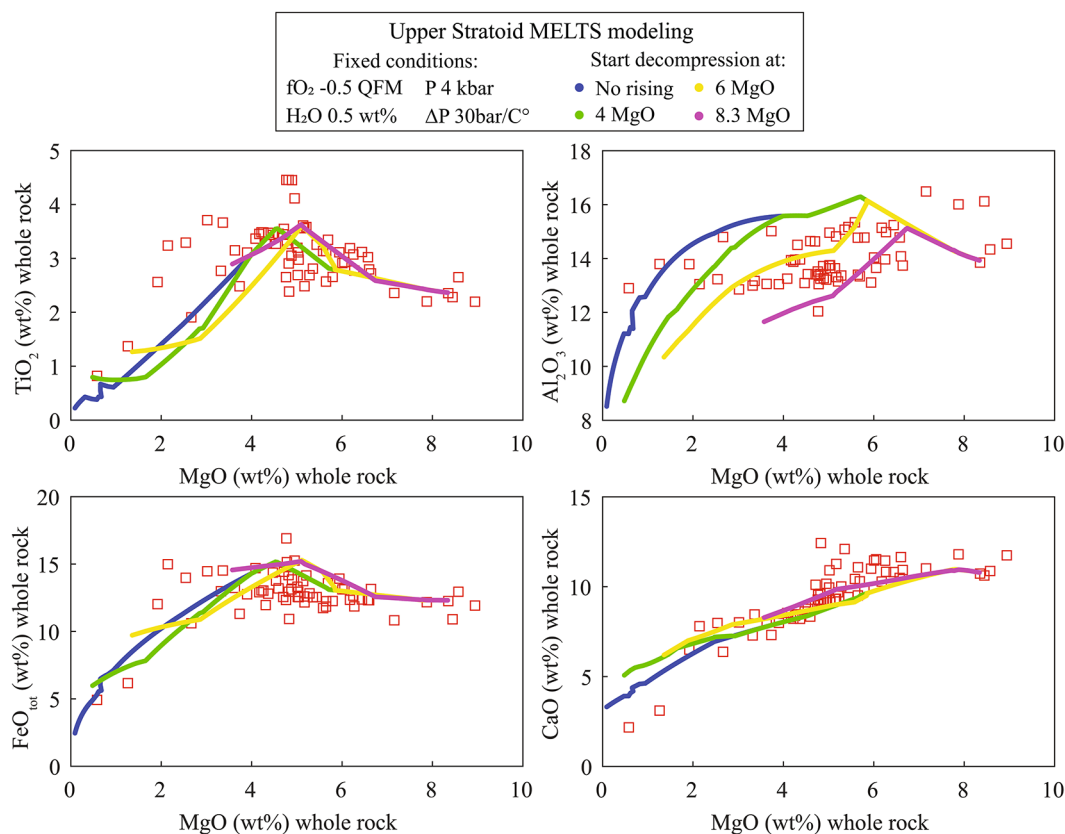
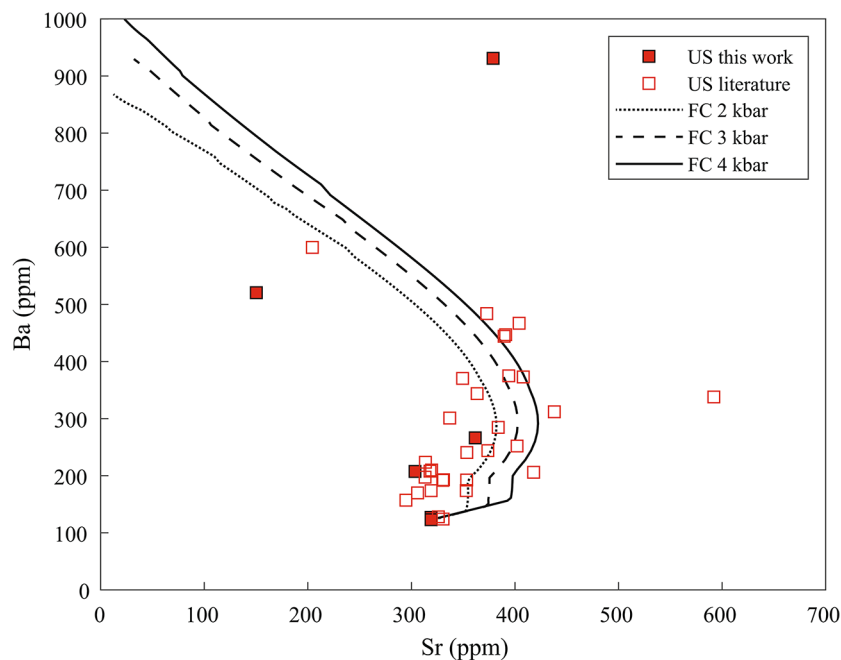


**Fig. 11** Best fit modeled liquid line of descent for the US Series major element by means of rhyolite-MELTS (Smith and Asimow 2005; Gualda et al. 2012). Using fixed oxygen fugacity (QFM -0.5) and starting water content (0.5 wt%), we model magma fractionate in the deep

reservoir (4 kbar) or start decompressing it at different degrees of evolution (8.3, 6 and 4 MgO wt%) at 30 bar/C° from 4 kbar up to the surface. Literature data are from Tortelli et al. (2022), Feyissa et al. (2019) and Barberi and Santacroce (1980). All the models are in Fig. S5

**Fig. 12** MCS modeling for the US Series Sr and Ba concentration in the whole rock. We used the most mafic sample (Z16) as starting material and the conditions of AlphaMELTS best fit (QFM -0.5, H<sub>2</sub>O 0.5 wt%). In order to account for the depth of crystallization variation, the pressure is variable (2, 3 and 4 kbar). The K<sub>d</sub> of Sr and Ba has been calculated using Dohmen and Blundy (2014) according to the most mafic and silicic plagioclase composition calculated by AlphaMELTS. In particular we used T 1170 C°, An 71 and melt SiO<sub>2</sub> 50 wt% for the mafic end-member (K<sub>d</sub>, Sr 1.78 and Ba 0.21) and T 850 C°, An 25 and melt SiO<sub>2</sub> 70 wt% (K<sub>d</sub>, Sr 6.15 and Ba 0.43)



clinopyroxene (i.e., Mg#, Cr<sub>2</sub>O<sub>3</sub>) to reconstruct magma evolution in relation to intensive (e.g. pressure, temperature, water content) or extensive (e.g. magma mixing, assimilation) parameters. To this purpose, we discussed and ruled out the effect of chemical diffusion and crystallization kinetics on element redistribution (see [Supplementary Text](#)). MgO variations in plagioclase have not been used for the interpretation due the complex effect of the An content on Mg crystal-melt partitioning coefficient (Mutch et al. 2022; [Supplementary Text](#)).

#### Fractional crystallization, plagioclase entrainment and crystal mush resorption recorded in the US crystals

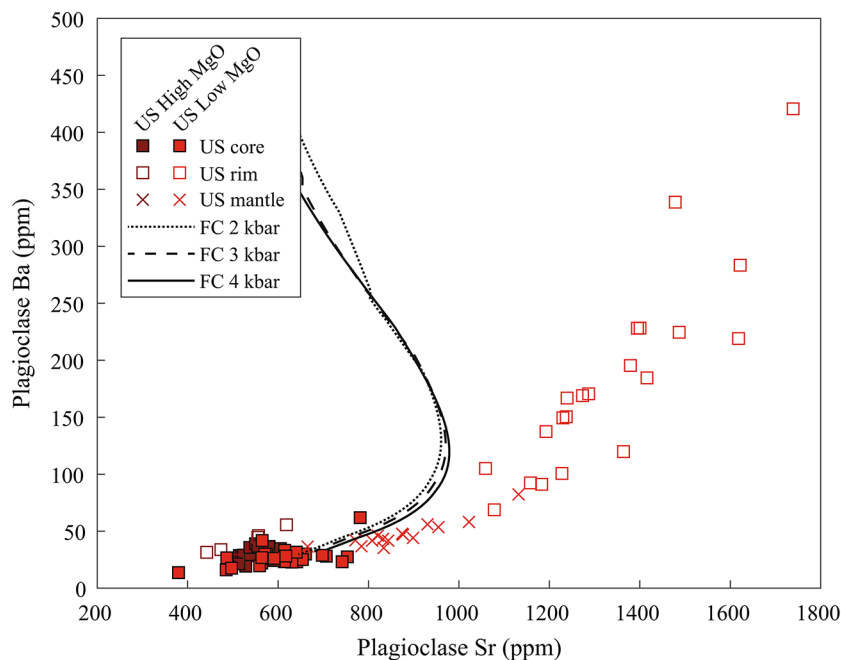
The plagioclase phenocrysts in the US high-MgO samples mostly show no variation in An, TiO<sub>2</sub> and FeO<sub>t</sub>, and no resorption features, suggesting that they grew in a stable and unperturbed magma reservoir (Fig. 5A; Type I in Fig. S3A). Few examples of increasing An with decreasing TiO<sub>2</sub> (Fig. S3A) record the occurrence of mafic refilling.

The plagioclase of the US low-MgO samples have cores with overall constant composition of An, TiO<sub>2</sub> and FeO<sub>t</sub>, indicating that the cores grew in a stable and unperturbed magma reservoir. However, resorbed cores which are sometimes sieve-textured have been observed (Fig. S3B), and at the core-rim transition an abrupt decrease in An is accompanied by an increase in FeO<sub>t</sub> and TiO<sub>2</sub> (Fig. 5B; Type II in Fig. S3B). Such decrease in the An content and increase in FeO<sub>t</sub> and TiO<sub>2</sub> can be explained by the high An plagioclase being entrained in the low MgO magma and crystallized the low An rim after a period of plagioclase dissolution, causing

the observed compositional gap (Figs. 3G and 5B; Type II in Fig. S3B). Furthermore, more complex zoning is observed in some plagioclase phenocrysts, such as decreasing in An coupled with the increasing TiO<sub>2</sub> and FeO from core to mantle or oscillations of An and, sometimes, also of TiO<sub>2</sub> (Fig. 5C; Type III in Fig. S3B). The core-mantle variations again suggest the crystal entering a more evolved magma while the oscillatory mantle could be explained by polybaric convection (e.g. Ustunisik et al. 2014) in a slightly zoned magmatic system (when An is coupled with TiO<sub>2</sub>) before being erupted.

Crystal entering and crystallizing in a more evolved magma can explain the increase of incompatible elements (Ba, LREE) in the plagioclase mantles and rims but not the observed increase of the Sr, up to 1740 ppm (Fig. 7A; Fig. S4). We therefore used the output of the MCS model (Fig. 12) to obtain the concentration of Sr and Ba in the plagioclase during fractional crystallization and plotted them in Fig. 13 together with the composition of natural US plagioclase. According to the model, fractional crystallization can only partially explain the increase in Sr in the plagioclase, without however explaining the highest concentrations (i.e., >1000 ppm; Fig. 13). We therefore model Recharge, Assimilation, and Fractional Crystallization (RAFC) with MCS using the high An plagioclase composition as an assimilant to evaluate if the assimilation of a plagioclase-rich wall rock can explain the high Sr concentrations. Despite the initial increase in Sr (up to ~850 ppm), the high solidus temperature of the plagioclase caused the magma and assimilant temperature to soon equalize, preventing MCS from continuing the modeling. However,

**Fig. 13** Comparison of plagioclase Sr and Ba analyzed in the US samples and the same elements modeled during fractional crystallization. The plagioclase modeled composition is calculated by MCS during the whole rock fractional crystallization modeling shown in Fig. 12, so the starting material, the condition used and the calculated  $K_d$  are the same. In order to account for the variation of crystallization depth, pressure conditions vary (2, 3 and 4 kbar). The results show that none of the model is able to reproduce the increase in Sr in plagioclase



magma mixing experiments of basaltic Icelandic lavas indicate that mixing-induced chemical disequilibrium can lead to plagioclase resorption (Neave et al. 2021; Nakamura and Shimakita 1998). Considering the strong chemical disequilibrium between the plagioclase core and the carrying magma, together with the textural evidence of resorption, it is reasonable to think that high An core dissolves in the low-MgO due to chemical disequilibrium. We therefore suggest that the plagioclase dissolution led to the enrichment of Sr in the melt that eventually crystallized the high Sr rim and mantle, similar to what is observed during the thermally remobilization of crystal mush in silicic magmatic systems (Forni et al. 2015; Wolff et al. 2015; Bachmann et al. 2014). At the same time, the absence of plagioclase crystallization would lead to an increase of Sr in the melt if associated with fractionation of other Sr-poor minerals. However, the enrichment in Sr is observed only in the plagioclase and not in the whole rock analysis (Fig. 12), suggesting the melt enrichment is volumetrically restricted. According to Neave et al. (2021), which indicate that even modest amounts of resorption could trigger mush disaggregation, we suggest the dissolution took place within the interstices, along grain boundaries, of mush-like portions that were later infiltrated and disaggregated by rising magma that, enriched in Sr due to plagioclase dissolution, crystallized the high-Sr rim just before or during eruption. In conclusion, based on our observations, the petrogenesis of the US magmas involves an initial period of fractional crystallization in a stable and unperturbed magma reservoir. Subsequently the evolution proceeds within a melt-rich moderately zoned magmatic system due to fractional crystallization and polybaric

convection. Eventually, the mineral-melt disequilibrium led to plagioclase dissolution and generation of Sr-rich melt in crystal mushes portions of the magmatic system.

#### Fractional crystallization, magma mixing and recharging events recorded in the CAG crystals

The plagioclase phenocrysts of the CAG high-MgO lavas are unzoned in An,  $\text{TiO}_2$  and  $\text{FeO}$ , suggesting they grow in an overall stable and unperturbed reservoir, similarly to US (Fig. 5D; Type I in Fig. S3C). On the contrary, petrographic evidence of variations in the crystal abundance and groundmass size suggest possible mixing events for the two analyzed CAG low-MgO samples (Fig. S1). Evidence of reverse zoning has been observed in plagioclase with sieved cores and increasing An and decreasing  $\text{TiO}_2$  in the mantle with respect to the cores (Fig. 5E; Type II in Fig. S3D). The sieved core may indicate disequilibrium induced by magma mixing, possibly due to the arrival of a Ca-rich and  $\text{TiO}_2$ -poor mafic magma in a more evolved reservoir, with consequent crystallization of the high-An mantle. More complex zoning is instead observed in some plagioclase with a core to mantle direct zoning (i.e., decrease in An and increase in  $\text{TiO}_2$ ) sometimes followed by a reversely zoned portion before the rims (i.e., increase in An and decrease in  $\text{TiO}_2$ ; Type III in Fig. S3D). This suggests that magma mixes with a more evolved melt and the low An plagioclase mantle crystallizes around the high An plagioclase core. At a later time, the same reservoir is affected by the arrival of a new mafic input. Small increase or decrease of An corresponding to inverse or no  $\text{TiO}_2$  variations could also suggest mixing

between two slightly different magmas (Fig. 5F; Type IV and V in Fig. S3D).

Recharging events are also suggested by some clinopyroxene profiles showing increase in Mg# and Cr<sub>2</sub>O<sub>3</sub> in the mantle and rim with respect to the core, indicating the arrival of more mafic magmas (Fig. 6). These observations indicate that, beside fractional crystallization, CAG reservoirs are affected by several recharging events and mixing between magmas with different degrees of evolution. The CAG clinopyroxene are chemically more variable and overall more enriched in TiO<sub>2</sub>, Al<sub>2</sub>O<sub>3</sub> and Na<sub>2</sub>O for the same Mg# content with respect to the US, suggesting higher chemical variability within the CAG with respect to the US (Fig. 7B; Fig. S2D, E,F). Furthermore, different trends between the two Series have been observed for Ni in olivine (Fig. S2G). These variations could be related to both mantle source and/or fractional crystallization processes. Investigating the nature of these differences is beyond the scope of this study and clinopyroxene trace elements analyses are needed for a comprehensive study. However, these observations emphasize the differences between the two series and also the variability of the CAG Series with respect to the more homogeneous US.

## Magmatic system architecture and dynamics

### The deep and stable magmatic system of the US volcanic phase

Most of the US lavas do not show evidence of shallow crystallization as, when the mineral-melt equilibrium is achieved, it is mostly at middle-lower crust levels (10–18 km), just below the upper-lower crust transition (Hammond et al. 2011). The geobarometry results do not show a clear distinction of high-MgO, low-MgO and silicic magmas in discrete reservoirs at different depths (Fig. 10). Based on density constraints, we therefore suggest that the US high-MgO magmas, with high Mg# pyroxene, Fo-rich olivine and plagioclase, the latter bearing evidence of mafic recharging events, reside in the deeper reservoir(s) of this middle-lower crustal magmatic system (Fig. 14A). Above these, in the shallower reservoir(s), we instead identify the low-MgO nearly aphyric magmas with sporadic high An plagioclase and low Mg# clinopyroxene and olivine that are mostly in disequilibrium with the host rock. Finally, we suggest that the silicic magmas, with low An plagioclase, form at the very top of this magmatic system (Fig. 14A).

It is reasonable that the high An plagioclase, found as cores (up to An<sub>88</sub>) in disequilibrium with the host low-MgO magma, crystallized from a high-MgO-like or more mafic magma in a deep-crustal magmatic system, possibly near the Moho and never directly tapped by eruptions (Fig. 14A).

The possibility of these high-An plagioclase floating in the deep magmatic system can be evaluated by density calculations. According to results from MELTS, the calculated liquid remains denser (2.76–2.71 g/cm<sup>3</sup>) with respect to the crystallized plagioclase (An<sub>71–64</sub>; 2.67–2.66 g/cm<sup>3</sup>) and also with respect to a bytownite composition (2.71 g/cm<sup>3</sup>), until the magma reaches ~3.8 MgO wt%. Furthermore, in the same MgO range, MELTS calculation indicates an overall low melt viscosity (7.4–31 Pa\*s). Using a mean of the liquid density (2.73 g/cm<sup>3</sup>) and viscosity (20 Pa\*s) and 1 mm size plagioclase of bytownite composition (2.71 g/cm<sup>3</sup>), the Stokes law suggest that plagioclase may remain buoyant in the deep mafic magma ( $-1.4 \times 10^{-6}$  m/s). The mafic minerals crystallized in the deep mafic magma (clinopyroxene and olivine, respectively 3.23 g/cm<sup>3</sup> and 3.24 g/cm<sup>3</sup>) are instead denser than the melt and therefore prone to sink.

The high An plagioclase can therefore be separated from the denser mafic minerals and carried up by magma ascending from the top of the deep-crustal magmatic system, while clinopyroxene and olivine mostly settle down. The ascent of differentiated magma, polybaric convection (Fig. 5B, C) and plagioclase buoyancy can therefore explain the presence of high An plagioclase in the shallower reservoir(s) of the middle-lower crustal magmatic system. At the same time, the rising plagioclase could be stored in a plagioclase-dominated crystal mush, at the top (but possibly also on the sides) of this middle-lower crustal magmatic system (Fig. 14A), as already proposed for several magmatic systems (e.g., Neave et al. 2014; Sheth 2016; Valer et al. 2017; Óskarsson et al. 2017; Marzoli et al. 2022). Still, we cannot exclude the possibility of in situ crystallization during earlier phases of the magmatic system. Nevertheless, we suggest that the mush forming at the top of the middle-lower crustal magmatic system could be responsible for the differentiation of the crystal-poor US low-MgO and silicic lavas, as already observed for several silicic magma reservoirs (Jackson et al. 2018; Forni et al. 2016; Dufek and Bachmann 2010). At the same time the chemical disequilibrium between the mush and the low-MgO magma percolating within the mush interstices drive the plagioclase resorption, leading to the formation of discrete melt portions enriched in Sr (Fig. 14A; Forni et al. 2015; Wolff et al. 2015; Bachmann et al. 2014) and favoring mush disaggregation (Neave et al. 2021). Eventually, when the shallower reservoir(s) get destabilized and the low-MgO magma eruption begins, the mush starts to disaggregate and the high-Sr melt located within the mush interstices starts to crystallize the Sr-rich rims of the ripped high An plagioclase. The paucity of clinopyroxene and olivine in the US suggest that they settled down to form a cumulated crystal mush at the base of the middle-lower crustal magmatic system, and only occasionally erupted with the high-MgO lava (Fig. 14A).



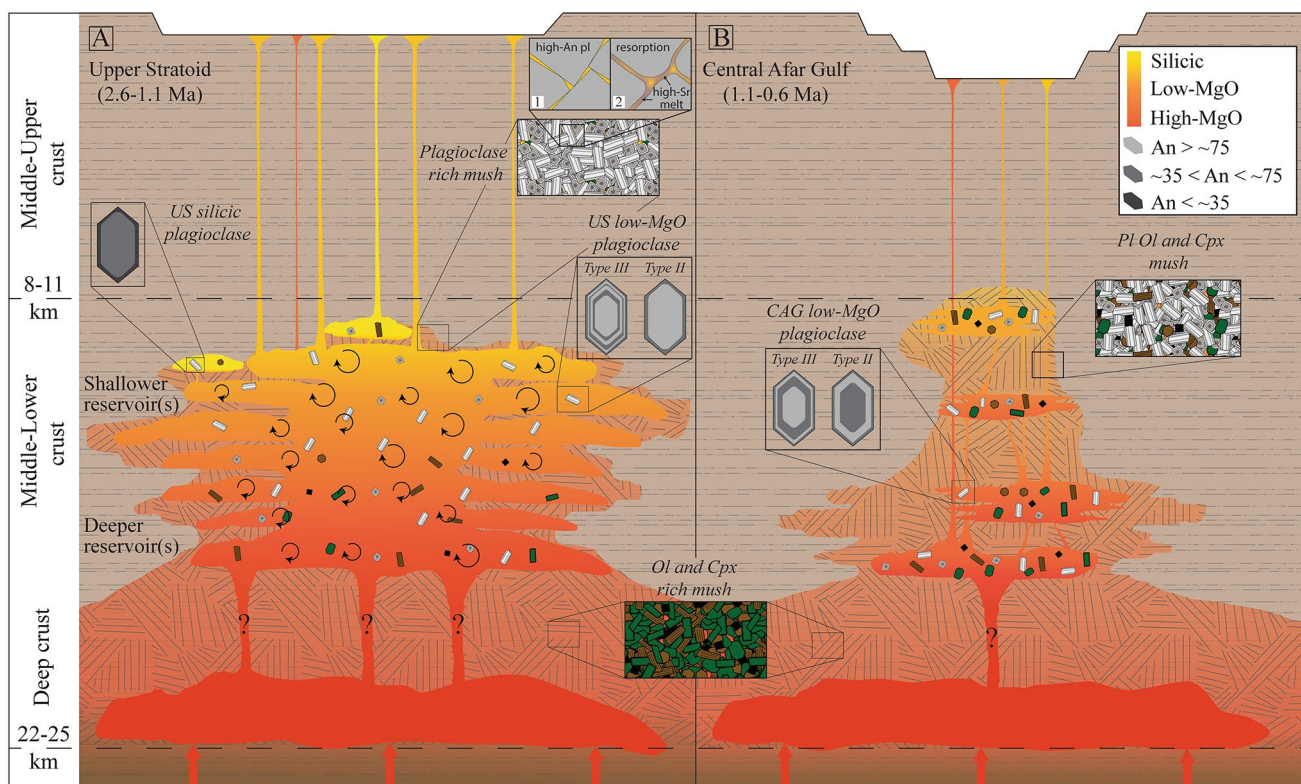


**Fig. 14** Schematic cartoon depicting the magmatic system of US and CAG in Central Afar. **(A)** The US scenario involves plagioclase rising from the deeper to the shallower reservoir(s) of a melt-dominated, middle-lower crustal magmatic system. In the shallower reservoir(s) a plagioclase-rich mush forms and the aphyric, mainly moderately evolved (i.e., low-MgO magma) is tapped for eruption, tearing plagioclase from the mush and rising directly to the surface. The mush inset shows the interstitial low-MgO magmas driving the resorption of the high An plagioclase (1) and the melt Sr-enrichment (2). Sporadically,

rhyolitic composition may be reached. Only occasionally the eruptions tapped the high-MgO magma of the deeper reservoir(s). **(B)** The CAG are dominated by a melt-poor magmatic system with respect to the US, with eruptions taking place tapping smaller, crystal-rich and interconnected magma chambers. The sketch is not to scale. The depth of the Moho and of the lower-upper crust limit are from Hammond et al. (2011). The plagioclase represents the main type used for the interpretation. See text for more details

### The polybaric and interconnected magmatic system for the CAG volcanic phase

The CAG show a marked decrease of erupted volumes with respect to the US, indicating a decrease of the eruptable melt stored in the crust. Relatively small magmatic reservoirs can therefore be envisaged for the CAG activity (Fig. 14B). The increase in porphyricity suggests instead that the CAG magmas are more crystal-rich with respect to the US while the more variable mineral assemblage indicates that crystals, in particular olivine and clinopyroxene, are not fractionated so efficiently as for the US (Fig. S1C). Evidence in both plagioclase and clinopyroxene of recharging events and magma mixing (Figs. 5E and 6; Type II in Fig. S3D) indicate that the small reservoirs of the CAG are interconnected (Fig. 14B). Furthermore, evidence of multiple recharging events suggested by phenocrysts with complex zoning (Type III in Fig. S3D) indicates that the system is highly dynamic with the possibility of multiple events of mixing before eruption. Lastly, the variability of CAG

clinopyroxene and olivine mineral chemistry (Fig. 7B; Fig. S2) argue for a more heterogeneous magmatic system with respect to the US.

### Red Sea rift localization: magmatic system and crustal evolution

The US range from 2.6 to 1.1 Ma without evidence of long breaks and are characterized by voluminous eruptions of similar mostly moderately evolved, aphyric or nearly aphyric magmas indicating a homogenous and melt-rich magmatic system. We suggest that most of the US magma rose directly to the surface from the shallower reservoir(s) of a middle-lower crustal magmatic system. The eruptions, possibly induced by volatiles exsolution as a consequence of differentiation and/or decompression (Black and Manga 2017), mainly tap the aphyric or low plagioclase-phyric low-MgO magma, tearing few plagioclase from the crystal mush. Only occasionally the eruptions tapped the high-MgO magma of the deeper reservoir(s) and the silicic magma of

the shallower reservoir(s) (Fig. 14A). This reconstruction is in agreement with evidence of magma differentiation taking place in the lower and middle crust (Sparks et al. 2019; Annen et al. 2006), and in general agreement with models of large eruption magmatic systems (Black and Manga 2017; Ernst et al. 2019; Karlstrom and Richards 2011).

At ~1 Ma, the CAG magmatic system developed at middle-lower crustal depths, similarly to the US. The highly dynamic CAG magmatic system with magma rising through multiple, relatively small, crystal-rich and interconnected reservoirs (Fig. 14) differ from the US and is instead similar to the one observed for the magmatic segments in Afar (Pagli et al. 2012; Desissa et al. 2013; Didana et al. 2014; Field et al. 2012a; Chambers et al. 2021; Biggs et al. 2021) and to the source-to-surface vertically stacked magmatic systems described in Cashman et al. (2017). Considering the decrease of erupted volume from the US to the CAG and the increase in the degree of partial melting (Tortelli et al. 2022), an important volume of intruded material at the US-CAG transition is required. This is in agreement with large volumes of intruded material and cumulates observed along the magmatic segments (Hutchison et al. 2018; Lewi et al. 2016). Moreover, Bridges et al. (2012) identified a 10 km wide zone of diking intruding the Tendaho graben in the last 0.8 Myrs of extension, corresponding in time and space with the CAG eruptive phase. We therefore suggest a transition from a melt-dominated magmatic system (i.e., US volcanic phase), to a stacked, crystal-rich magmatic system which started forming since the rift began to localize (i.e., CAG volcanic phase) and whose magmatic architecture is comparable with the present-day magmatic segments activity in Afar.

The link between rift processes and related volcanism have been studied elsewhere, such as the North Atlantic Igneous Province associated with the opening of the North Atlantic ocean and extending between Greenland, Iceland, the Faroe Islands and the northwest British Isles (e.g., Saunders et al. 1997). The US shows similarities with the Neogene flood basalts of eastern Iceland, which precede the ongoing rifting activity of the Iceland oceanic ridge and are dominated by aphyric magma (50–70%) and, to a lesser extent, by plagioclase- or olivine-phyric magmas (Walker 1958). In particular, our reconstruction of the US magmatic system architecture and mush disaggregation process occurring in the middle-lower crust is very similar to the one proposed for the Neogene flood basalt -Grænavatn formation- (Óskarsson et al. 2017). Following the widespread volcanic eruption, the stacked and interconnected CAG magmatic system is instead comparable with the one observed for the magmatic segments in Iceland (Neave et al. 2013; Caracciolo et al. 2023).

## Conclusions

The transition from the Upper Stratoid to the Central Afar Gulf volcanic activity represents a crucial stage of rift evolution, marking the transition from broad to localized rift in Central Afar. By means of whole rock analysis, major and trace element mineral chemistry, geothermobarometry estimates and geochemical modeling for both whole rock and mineral chemistry, we identify contrasting magmatic system architectures for the Upper Stratoid and the Central Afar Gulf, which helps to interpret magmatic system evolution during the continental breakup.

The Upper Stratoid evolved due to fractional crystallization in a melt-dominated, slightly zoned, middle-lower crust (10–18 km) magmatic system. Polybaric plagioclase convection and dissolution of a plagioclase-rich crystal mush is recorded in the phenocryst texture and chemistry. Magma mostly rose from the shallower portions of this magmatic system directly to the surface. The Central Afar Gulf magmatic system was instead crystal-rich, spanning approximately the same depth interval as that for the Upper Stratoid but dominated by multiple, relatively small and interconnected magmatic reservoirs. Unlike the Upper Stratoid, multiple mixing events between magmas with different degrees of evolution were frequent.

Our study documents the transition during the continental breakup from an overall stable and melt-rich magmatic system feeding the voluminous and homogeneous Upper Stratoid eruptions to a more dynamic, interconnected and crystal-rich situation feeding small-volume eruption while the rift localizes.

**Supplementary Information** The online version contains supplementary material available at <https://doi.org/10.1007/s00410-024-02164-7>.

**Acknowledgements** The research is part of the PhD of G. Tortelli and is funded by 2017 PRIN project-protocol MIUR: 2017P9AT72 PE10. G. Tortelli acknowledges support by the Tuscany Regional PhD Course in Earth Sciences. The authors are grateful to Gordon Moore, Editor of Contribution to Mineralogy and Petrology for handling the manuscript and to Thomas R. Hudgins and an anonymous reviewer for their valuable comments. We thank R. Ishak and M. Gemelli (SEM lab., CISUP, University of Pisa), A. Orlando (EPMA lab., CNR-IGG of Firenze) and M. Masotta (LA-ICP-MS lab., CISUP, University of Pisa) for their support during analytical acquisition. We thank R. Santacroce (University of Pisa) for discussions and support. We thank the colleagues of the Addis Ababa University and the Ethiopian and Afar Regional Governments, the drivers of the rental agency Ethioder, and the local policeman and guides of the different woredas for their support and logistic help in organizing and conducting the February 2020 campaign. Open access funding provided by Università di Firenze within the CRUI-CARE Agreement.

**Funding** Open access funding provided by Università degli Studi di Firenze within the CRUI-CARE Agreement.

**Data availability** The authors confirm that the data supporting this study is available within the online supplementary materials.

**Open Access** This article is licensed under a Creative Commons Attribution 4.0 International License, which permits use, sharing, adaptation, distribution and reproduction in any medium or format, as long as you give appropriate credit to the original author(s) and the source, provide a link to the Creative Commons licence, and indicate if changes were made. The images or other third party material in this article are included in the article's Creative Commons licence, unless indicated otherwise in a credit line to the material. If material is not included in the article's Creative Commons licence and your intended use is not permitted by statutory regulation or exceeds the permitted use, you will need to obtain permission directly from the copyright holder. To view a copy of this licence, visit <http://creativecommons.org/licenses/by/4.0/>.

## References

- Ahmed A, Doubre C, Leroy S, Keir D, Pagli C, Hammond JOS, Ayele A, Be de Berc M, Grunberg M, Vergne J, Pestourie R, Mamo D, Kibret B, Cubas N, Lavayssière A, Janowski M, Lengliné O, La Rosa A, Chambers EL, Illsley-Kemp F (2022) Across and along-strike crustal structure variations of the western Afar Margin and adjacent plateau: insights from receiver functions analysis. *J Afr Earth Sc* 192:104570. <https://doi.org/10.1016/j.jafrearsci.2022.104570>
- Annen C, Blundy JD, Sparks RSJ (2006) The Genesis of Intermediate and Silicic Magmas in Deep Crustal Hot zones. *J Petrol* 47:505–539. <https://doi.org/10.1093/petrology/egi084>
- Bachmann O, Deering CD, Lipman PW, Plummer C (2014) Building zoned ignimbrites by recycling silicic cumulates: insight from the 1,000 km<sup>3</sup> Carpenter Ridge Tuff, CO. *Contrib Miner Petrol* 167:1–13. <https://doi.org/10.1007/s00410-014-1025-3>
- Barberi F, Santacrose R (1980) The Afar Stratoid Series and the magmatic evolution of east African rift system. *Bull De La Société Géologique De France S7-XXII* 891:899. <https://doi.org/10.2113/gssgfbull.S7-XXII.6.891>
- Bastow ID, Keir D (2011) The protracted development of the continent–ocean transition in Afar. *Nat Geosci* 4:248–250. <https://doi.org/10.1038/ngeo1095>
- Bastow ID, Booth AD, Corti G, Keir D, Magee C, Jackson CAL, Warren J, Wilkinson J, Lascialfari M (2018) The development of late-stage Continental Breakup: seismic reflection and Borehole evidence from the Danakil Depression. *Ethiopia Tectonics* 37:2848–2862. <https://doi.org/10.1029/2017TC004798>
- Best MG (2013) *Igneous and metamorphic petrology*. Wiley
- Biggs J, Ayele A, Fischer TP, Fontijn K, Hutchison WR, Kazimoto EO, Whaler K, Wright T (2021) Volcanic activity and hazard in the East African Rift Zone. *Nat Commun* 12(1):6881. <https://doi.org/10.1038/s41467-021-27166-y>
- Bizouard H, Barberi F, Varet J (1980) Mineralogy and Petrology of Erta Ale and Boina Volcanic Series, Afar Rift, Ethiopia. *J Petrol* 21:401–436. <https://doi.org/10.1093/petrology/21.2.401>
- Black BA, Manga M (2017) Volatiles and the tempo of flood basalt magmatism. *Earth Planet Sci Lett* 458:130–140. <https://doi.org/10.1016/j.epsl.2016.09.035>
- Bohrson WA, Spera FJ, Heinonen JS, Brown GA, Scruggs MA, Adams JV, Takach MK, Zeff G, Suikkanen E (2020) Diagnosing open-system magmatic processes using the Magma Chamber Simulator (MCS): part I—major elements and phase equilibria. *Contrib Miner Petrol* 175:1–29. <https://doi.org/10.1007/s00410-020-01722-z>
- Bosworth W, Huchon P, McClay K (2005) The Red Sea and Gulf of Aden basins. *J Afr Earth Sc* 43:334–378. <https://doi.org/10.1016/j.jafrearsci.2005.07.020>
- Bridges DL, Mickus K, Gao SS, Abdelsalam MG, Alemu A (2012) Magnetic stripes of a transitional continental rift in Afar. *Geology* 40:203–206. <https://doi.org/10.1130/G32697.1>
- Brune S, Kolawole F, Olive J, Stamps DS, Buck WR, Buitter S, Furman T, Shillington DJ (2023) Geodynamics of continental rift initiation and evolution. *Nat Reviews Earth Environ* 4(4):235–253. <https://doi.org/10.1038/s43017-023-00391-3>
- Caracciolo A, Bali E, Halldórsson SA, Guðfinnsson GH, Kahl M, Þórðardóttir I, Pálmadóttir GL, Silvestri V (2023) Magma plumbing architectures and timescales of magmatic processes during historical magmatism on the Reykjanes Peninsula, Iceland. *Earth Planet Sci Lett* 621:118378. <https://doi.org/10.1016/j.epsl.2023.118378>
- Cashman KV, Sparks RSJ, Blundy JD (2017) Vertically extensive and unstable magmatic systems: a unified view of igneous processes. *Science* 355:eaag3055. <https://doi.org/10.1126/science.aag3055>
- Chambers EL, Harmon N, Rychert CA, Keir D (2021) Variations in melt emplacement beneath the northern east African rift from radial anisotropy. *Earth Planet Sci Lett* 573:117150. <https://doi.org/10.1016/j.epsl.2021.117150>
- Cochran JR (1983) A model for development of Red Sea I. *AAPG Bull* 67:41–69. <https://doi.org/10.1306/03B5ACBE-16D1-11D7-8645000102C1865D>
- de Moor JM, Fischer TP, Sharp ZD, King PL, Wilke M, Botcharnikov RE, Cottrell E, Zelenski M, Marty B, Klimm K, Rivard C, Ayalew D, Ramirez C, Kelley KA (2013) Sulfur degassing at Erta Ale (Ethiopia) and Masaya (Nicaragua) volcanoes: implications for degassing processes and oxygen fugacities of basaltic systems. *Geochem Geophys Geosyst* 14:4076–4108. <https://doi.org/10.1002/ggge.20255>
- Desissa M, Johnson NE, Whaler KA, Hautot S, Fisseha S, Dawes GJK (2013) A mantle magma reservoir beneath an incipient mid-ocean ridge in Afar, Ethiopia. *Nat Geosci* 6:861–865. <https://doi.org/10.1038/ngeo1925>
- Didana YL, Thiel S, Heinson G (2014) Magnetotelluric imaging of upper crustal partial melt at Tendaho Graben in Afar, Ethiopia. *Geophys Res Lett* 41:3089–3095. <https://doi.org/10.1002/2014GL060000>
- Dostal J, Hamilton TS, Shellnutt JG (2017) Generation of felsic rocks of bimodal volcanic suites from thinned and rifted continental margins: Geochemical and Nd, Sr, Pb-isotopic evidence from Haida Gwaii, British Columbia, Canada. *Lithos* 292:146–160. <https://doi.org/10.1016/j.lithos.2017.09.005>
- Dufek J, Bachmann O (2010) Quantum magmatism: magmatic compositional gaps generated by melt-crystal dynamics. *Geology* 38:687–690. <https://doi.org/10.1130/G30831.1>
- Ebinger CJ, Casey M (2001) Continental breakup in magmatic provinces: an Ethiopian example. *Geology* 29(6):527–530. [https://doi.org/10.1130/0091-7613\(2001\)029<0527:CBIMPA>2.0.CO;2](https://doi.org/10.1130/0091-7613(2001)029<0527:CBIMPA>2.0.CO;2)
- Ebinger CJ, Yemane T, Woldegabriel G, Aronson JL, Walter RC (1993) Late eocene–recent volcanism and faulting in the southern main Ethiopian rift. *J Geol Soc* 150:99–108. <https://doi.org/10.1144/gsjgs.150.1.0099>
- Ernst RE, Liikane DA, Jowitt SM, Buchan KL, Blanchard JA (2019) A new plumbing system framework for mantle plume-related continental large igneous provinces and their mafic-ultramafic intrusions. *J Volcanol Geoth Res* 384:75–84. <https://doi.org/10.1016/j.jvolgeores.2019.07.007>
- Ferguson DJ, Calvert AT, Pyle DM, Blundy JD, Yirgu G, Wright TJ (2013) Constraining timescales of focused magmatic accretion and extension in the Afar crust using lava geochronology. *Nat Commun* 4(1):1416. <https://doi.org/10.1038/ncomms2410>
- Feyissa DH, Kitagawa H, Bizuneh TD, Tanaka R, Kabeto K, Nakamura E (2019) Transition from plume-driven to plate-driven

- Magmatism in the evolution of the Main Ethiopian Rift. *J Petrol* 60:1681–1715. <https://doi.org/10.1093/petrology/egz043>
- Field L, Blundy J, Brooker RA, Wright T, Yirgu G (2012a) Magma storage conditions beneath Dabbahu Volcano (Ethiopia) constrained by petrology, seismicity and satellite geodesy. *Bull Volcanol* 74:981–1004. <https://doi.org/10.1007/s00445-012-0580-6>
- Field L, Barnie T, Blundy J, Brooker RA, Keir D, Lewi E, Saunders K (2012b) Integrated field, satellite and petrological observations of the November 2010 eruption of Erta Ale. *Bull Volcanol* 74:2251–2271. <https://doi.org/10.1007/s00445-012-0660-7>
- Field L, Blundy J, Calvert A, Yirgu G (2013) Magmatic history of Dabbahu, a composite volcano in the Afar Rift, Ethiopia. *Geol Soc Am Bull* 125:128–147. <https://doi.org/10.1130/B30560.1>
- Fitton JG, Saunders AD, Larsen LM, Hardarson BS, Norry MJ (1998) Volcanic rocks from the southeast Greenland Margin at 63°N: composition, petrogenesis, and mantle sources. *Proceedings of the Ocean Drilling Program. Scientific results, vol. 152, pp. 331–350. Ocean Drilling Program, 1998.* <https://doi.org/10.2973/odp.proc.sr.152.233.1998>
- Forni F, Ellis BS, Bachmann O, Lucchi F, Tranne CA, Agostini S, Dallai L (2015) Erupted cumulate fragments in rhyolites from Lipari (Aeolian Islands). *Contrib Miner Petrol* 170:1–18. <https://doi.org/10.1007/s00410-015-1201-0>
- Forni F, Bachmann O, Mollo S, De Astis G, Gelman SE, Ellis BS (2016) The origin of a zoned ignimbrite: insights into the Campanian Ignimbrite magma chamber (Campi Flegrei, Italy). *Earth Planet Sci Lett* 449:259–271. <https://doi.org/10.1016/j.epsl.2016.06.003>
- Fournier M, Petit C, Huchon P, D'acremont E, Lepvrier C, Leroy S, Chamot-Rooke N, Al-Kathiri A, Audin L, Beslier MO, Fabbri O, Fleury JM, Khanbari K, Maillot B, Merkouriev S (2010) Arabia-Somalia plate kinematics, evolution of the Aden-OwenCarlsberg triple junction, and opening of the Gulf of Aden. *J Geophys Research: Solid Earth* 115(B4). <https://doi.org/10.1029/2008JB006257>
- Fowler SJ, Bohrsen WA, Spera FJ (2004) Magmatic evolution of the Skye igneous centre, western Scotland: modelling of assimilation, recharge and fractional crystallization. *J Petrol* 45(12):2481–2505. <https://doi.org/10.1093/petrology/egh074>
- Franceschini Z, Cioni R, Scaillet S, Corti G, Sani F, Isola I, Mazzarini F, Duval F, Erbello A, Muluneh A, Brune S (2020) Recent volcano-tectonic activity of the Ririba rift and the evolution of rifting in South Ethiopia. *J Volcanol Geoth Res* 403:106989. <https://doi.org/10.1016/j.jvolgeores.2020.106989>
- Goswami S, Dey S, Zakaulla S, Verma MB (2020) Active rifting and bimodal volcanism in Proterozoic Papaghni sub-basin, Cuddapah basin (Andhra Pradesh), India. *J Earth Syst Sci* 129:1–31. <https://doi.org/10.1007/s12040-019-1278-3>
- Grandin R, Socquet A, Doin MP, Jacques E, De Chabaliere JB, King GCP (2010) Transient rift opening in response to multiple dike injections in the Manda Hararo rift (Afar, Ethiopia) imaged by time-dependent elastic inversion of interferometric synthetic aperture radar data. *J Geophys Research: Solid Earth* 115(B9). <https://doi.org/10.1029/2009JB006883>
- Gualda GAR, Ghiorso MS, Lemons RV, Carley TL (2012) Rhyolite-MELTS: a modified calibration of MELTS optimized for silica-rich, fluid-bearing magmatic systems. *J Petrol* 53:875–890. <https://doi.org/10.1093/petrology/egr080>
- Hammond JOS (2014) Constraining melt geometries beneath the Afar Depression, Ethiopia from teleseismic receiver functions: the anisotropic H- $\kappa$  stacking technique. *Geochem Geophys Geosyst* 15:1316–1332. <https://doi.org/10.1002/2013GC005186>
- Hammond JOS, Kendall JM, Stuart GW, Keir D, Ebinger C, Ayele A, Belachew M (2011) The nature of the crust beneath the Afar triple junction: evidence from receiver functions. *Geochem Geophys Geosyst* 12. <https://doi.org/10.1029/2011GC003738>
- Heinonen JS, Bohrsen WA, Spera FJ, Brown GA, Scruggs MA, Adams JV (2020) Diagnosing open-system magmatic processes using the Magma Chamber Simulator (MCS): part II—trace elements and isotopes. *Contrib Miner Petrol* 175:1–21. <https://doi.org/10.1007/s00410-020-01718-9>
- Hofmann C, Courtillot V, Féraud G, Rochette P, Yirgu G, Ketefo E, Pik R (1997) Timing of the Ethiopian flood basalt event and implications for plume birth and global change. *Nature* 389:838–841. <https://doi.org/10.1038/39853>
- Hutchison WR, Mather TA, Pyle DM, Boyce AJ, Gleeson M, Yirgu G, Blundy J, Ferguson D, Vye-Brown C, Millar IL, Sims KW, Finch AA (2018) The evolution of magma during continental rifting: new constraints from the isotopic and trace element signatures of silicic magmas from Ethiopian volcanoes. *Earth Planet Sci Lett* 489:203–218. <https://doi.org/10.1016/j.epsl.2018.02.027>
- Jackson MD, Blundy J, Sparks RSJ (2018) Chemical differentiation, cold storage and remobilization of magma in the Earth's crust. *Nature* 564:405–409. <https://doi.org/10.1038/s41586-018-0746-2>
- Kalb JE (1995) Fossil elephantoids, awash paleolake basins, and the Afar triple junction. *Ethiopia Palaeogeography Palaeoclimatology Palaeoecology* 114:357–368. [https://doi.org/10.1016/0031-0182\(94\)00088-P](https://doi.org/10.1016/0031-0182(94)00088-P)
- Karlstrom L, Richards M (2011) On the evolution of large ultramafic magma chambers and timescales for flood basalt eruptions. *J Geophys Research: Solid Earth* 116(B8). <https://doi.org/10.1029/2010JB008159>
- Kidane T, Courtillot V, Manighetti I, Audin L, Lahitte P, Quidelleur X, Gillot PY, Gallet Y, Carlot J, Haile T (2003) New paleomagnetic and geochronologic results from Ethiopian Afar: Block rotations linked to rift overlap and propagation and determination of a ~2 Ma reference pole for stable Africa. *J Geophys Research: Solid Earth* 108(B2). <https://doi.org/10.1029/2001JB000645>
- La Rosa A, Pagli C, Wang H, Sigmundsson F, Pinel V, Keir D (2024) Simultaneous rift-scale inflation of a deep crustal sill network in Afar, East Africa. *Nat Commun* 15(1):4287. <https://doi.org/10.1038/s41467-024-47136-4>
- Lahitte P, Gillot PY, Courtillot V (2003a) Silicic central volcanoes as precursors to rift propagation: the Afar case. *Earth Planet Sci Lett* 207:103–116. [https://doi.org/10.1016/S0012-821X\(02\)01130-5](https://doi.org/10.1016/S0012-821X(02)01130-5)
- Lahitte P, Gillot PY, Kidane T, Courtillot V, Bekele A (2003b) New age constraints on the timing of volcanism in central Afar, in the presence of propagating rifts. *J Geophys Research: Solid Earth* 108(B2). <https://doi.org/10.1029/2001JB001689>
- Le Gall B, Daoud MA, Maury R, Gasse F, Rolet J, Jalludin M, Caminiti AM, Moussa N (2015) Carte géologique De La République De Djibouti. Cent. d'Etude Rech. Djibouti CCGM
- Lewi E, Keir D, Birhanu Y, Blundy J, Stuart G, Wright T, Calais E (2016) Use of a high-precision gravity survey to understand the formation of oceanic crust and the role of melt at the southern Red Sea rift in Afar, Ethiopia. *Special Publications* 420(1):165–180. <https://doi.org/10.1144/SP420.13>
- Marzoli A, Renne PR, Andreasen R, Spiess R, Chiaradia M, Ruth DC, Tholt AJ, Pande K, Costa F (2022) The shallow magmatic plumbing system of the Deccan traps, evidence from plagioclase megacrysts and their host lavas. *J Petrol* 63(9):egac075. <https://doi.org/10.1093/petrology/egac075>
- Medynski S, Pik R, Burnard P, Vye-Brown C, France L, Schimmelpfennig I, Whaler K, Johnson N, Benedetti L, Ayelew D, Yirgu G (2015) Stability of rift axis magma reservoirs: spatial and temporal evolution of magma supply in the Dabbahu rift segment (Afar, Ethiopia) over the past 30 kyr. *Earth Planet Sci Lett* 409:278–289. <https://doi.org/10.1016/j.epsl.2014.11.002>
- Mohr P, Girmius A, Rolff J (1978) Present-day strain rates at the northern end of the Ethiopian rift valley. *Tectonophysics* 44(1–4):141–160. [https://doi.org/10.1016/0040-1951\(78\)90067-7](https://doi.org/10.1016/0040-1951(78)90067-7)

- Muirhead JD, Kattenhorn SA, Lee H, Mana S, Turrin BD, Fischer TP, Kianji G, Dindi E, Stamps DS (2016) Evolution of upper crustal faulting assisted by magmatic volatile release during early-stage continental rift development in the East African Rift. *Geosphere* 12(6):1670–1700. <https://doi.org/10.1130/GES01375.1>
- Mutch EJF, Maclennan J, Madden-Nadeau AL (2022) The dichotomous nature of mg partitioning between plagioclase and melt: implications for diffusion chronometry. *Geochim Cosmochim Acta* 339:173–189. <https://doi.org/10.1016/j.gca.2022.10.035>
- Nakamura M, Shimakita S (1998) Dissolution origin and syn-entrapment compositional change of melt inclusion in plagioclase. *Earth Planet Sci Lett* 161(1–4):119–133. [https://doi.org/10.1016/S0012-821X\(98\)00144-7](https://doi.org/10.1016/S0012-821X(98)00144-7)
- Natali C, Beccaluva L, Bianchini G, Siena F (2011) Rhyolites associated to Ethiopian CFB: clues for initial rifting at the Afar plume axis. *Earth Planet Sci Lett* 312(1–2):59–68. <https://doi.org/10.1016/j.epsl.2011.09.059>
- Neave DA, Putirka KD (2017) A new clinopyroxene-liquid barometer, and implications for magma storage pressures under Icelandic rift zones. *Am Mineral* 102:777–794. <https://doi.org/10.2138/am-2017-5968>
- Neave DA, Passmore E, Maclennan J, Fitton G, Thordarson T (2013) Crystal–melt relationships and the record of deep mixing and crystallization in the ad 1783 Laki Eruption, Iceland. *J Petrol* 54(8):1661–1690. <https://doi.org/10.1093/petrology/egt027>
- Neave DA, Maclennan J, Hartley ME, Edmonds M, Thordarson T (2014) Crystal storage and transfer in basaltic systems: the Skugafjöll eruption, Iceland. *J Petrol* 55(12):2311–2346. <https://doi.org/10.1093/petrology/egu058>
- Neave DA, Beckmann P, Behrens H, Holtz F (2021) Mixing between chemically variable primitive basalts creates and modifies crystal cargoes. *Nat Commun* 12(1):5495. <https://doi.org/10.1038/s41467-021-25820-z>
- Nicotra E, Viccaro M, Donato P, Acocella V, De Rosa R (2021) Catching the Main Ethiopian Rift evolving towards plate divergence. *Sci Rep* 11(1):21821. <https://doi.org/10.1038/s41598-021-01259-6>
- Óskarsson BV, Andersen CB, Riisshuus MS, Sørensen EV, Tegner C (2017) The mode of emplacement of Neogene flood basalts in Eastern Iceland: the plagioclase ultraphyric basalts in the Grænavatn group. *J Volcanol Geoth Res* 332:26–50. <https://doi.org/10.1016/j.jvolgeores.2017.01.006>
- Pagli C, Wright TJ, Ebinger CJ, Yun SH, Cann JR, Barnie T, Ayele A (2012) Shallow axial magma chamber at the slow-spreading Erta Ale Ridge. *Nat Geosci* 5:284–288. <https://doi.org/10.1038/ngo1414>
- Paton C, Hellstrom J, Paul B, Woodhead J, Hergt J (2011) Iolite: Free-ware for the visualisation and processing of mass spectrometric data. *J Anal Spectrom* 26:2508–2518. <https://doi.org/10.1039/C1JA10172B>
- Pik R, Deniel C, Coulon C, Yirgu G, Marty B (1999) Isotopic and trace element signatures of Ethiopian flood basalts: evidence for plume–lithosphere interactions. *Geochim Cosmochim Acta* 63(15):2263–2279. [https://doi.org/10.1016/S0016-7037\(99\)00141-6](https://doi.org/10.1016/S0016-7037(99)00141-6)
- Poucllet A, El Hadi H, Álvaro JJ, Bardintzeff JM, Benharref M, Fekkek A (2018) Review of the Cambrian volcanic activity in Morocco: geochemical fingerprints and geotectonic implications for the rifting of West Gondwana. *Int J Earth Sci* 107:2101–2123. <https://doi.org/10.1007/s00531-018-1590-1>
- Putirka KD (2008) Thermometers and barometers for Volcanic systems. *Rev Mineral Geochem* 69:61–120. <https://doi.org/10.2138/rmg.2008.69.3>
- Rime V, Foubert A, Ruch J, Kidane T (2023) Tectonostratigraphic evolution and significance of the Afar Depression. *Earth Sci Rev* 104519. <https://doi.org/10.1016/j.earscirev.2023.104519>
- Rooney TO (2017) The cenozoic magmatism of East-Africa: Part I—Flood basalts and pulsed magmatism. *Lithos* 286:264–301. <https://doi.org/10.1016/j.lithos.2017.05.014>
- Rooney TO (2020a) The cenozoic magmatism of East Africa: part II—Rifting of the mobile belt. *Lithos* 360:105291. <https://doi.org/10.1016/j.lithos.2019.105291>
- Rooney TO (2020b) The cenozoic magmatism of East Africa: part IV—the terminal stages of rifting preserved in the Northern East African Rift System. *Lithos* 360:105381. <https://doi.org/10.1016/j.lithos.2020.105381>
- Rooney TO, Brown EL, Bastow ID, Arrowsmith JR, Campisano CJ (2023) Magmatism during the continent–ocean transition. *Earth Planet Sci Lett* 614:118189. <https://doi.org/10.1016/j.epsl.2023.118189>
- Saunders AD, Fitton JG, Kerr AC, Norry MJ, Kent RW, Mahoney JJ, Coffin MF (1997) The north Atlantic igneous province. *Geophys Monograph-American Geophys Union* 100:45–94. <https://doi.org/10.1029/GM100p0045>
- Sheth H (2016) Giant plagioclase basalts: Continental flood basalt-induced remobilization of anorthositic mushes in a deep crustal sill complex. *Bulletin* 128(5–6):916–925. <https://doi.org/10.1130/B31404.1>
- Shillington DJ, Scott CL, Minshull TA, Edwards RA, Brown PJ, White N (2009) Abrupt transition from magma-starved to magma-rich rifting in the eastern Black Sea. *Geology* 37(1):7–10. <https://doi.org/10.1130/G25302A.1>
- Siegburg M, Gernon TM, Bull JM, Keir D, Barfod DN, Taylor RN, Abebe B, Ayele A (2018) Geological evolution of the Boset-Bericha volcanic complex, Main Ethiopian Rift: 40Ar/39Ar evidence for episodic pleistocene to Holocene Volcanism. *J Volcanol Geoth Res* 351:115–133. <https://doi.org/10.1016/j.jvolgeores.2017.12.014>
- Smith P, Asimow P (2005) AdiaBAT\_1ph: a new public front-end to the MELTS, pMELTS, and pHMELTS models. *Geochem Geophys Geosyst* 6. <https://doi.org/10.1029/2004GC000816>
- Sparks RSJ, Annen C, Blundy JD, Cashman KV, Rust AC, Jackson MD (2019) Formation and dynamics of magma reservoirs. *Philosophical Trans Royal Soc A: Math Phys Eng Sci* 377:20180019. <https://doi.org/10.1098/rsta.2018.0019>
- Stab M, Bellahsen N, Pik R, Quidelleur X, Ayalew D, Leroy S (2016) Modes of rifting in magma-rich settings: Tectono-magmatic evolution of Central Afar: modes of Rifting in Magma-Rich settings. *Tectonics* 35:2–38. <https://doi.org/10.1002/2015TC003893>
- Storch B, Haase KM, Romer RHW, Beier C, Koppers AAP (2020) Rifting of the oceanic Azores Plateau with episodic volcanic activity. *Sci Rep* 10(1):19718. <https://doi.org/10.1038/s41598-020-76691-1>
- Su X, Peng P, Foley S, Teixeira W, Zhai MG (2021) Initiation of continental breakup documented in evolution of the magma plumbing system of the ca. 925 Ma Dashigou large igneous province, North China. *Lithos* 384:105984. <https://doi.org/10.1016/j.lithos.2021.105984>
- Tortelli G, Gioncada A, Pagli C, Braschi E, Gebru EF, Keir D (2022) Constraints on the Magma Source and Rift Evolution From Geochemistry of the Stratoid Flood Basalts (Afar, Ethiopia). *Geochemistry, Geophysics, Geosystems* 23 e2022GC010434. <https://doi.org/10.1029/2022GC010434>
- Ukstins IA, Renne PR, Wolfenden E, Baker J, Ayalew D, Menzies M (2002) Matching conjugate volcanic rifted margins: 40Ar/39Ar chrono-stratigraphy of pre-and syn-rift bimodal flood volcanism in Ethiopia and Yemen. *Earth Planet Sci Lett* 198(3–4):289–306. [https://doi.org/10.1016/S0012-821X\(02\)00525-3](https://doi.org/10.1016/S0012-821X(02)00525-3)
- Ustunisik G, Kilinc A, Nielsen RL (2014) New insights into the processes controlling compositional zoning in plagioclase. *Lithos* 200–201:80–93. <https://doi.org/10.1016/j.lithos.2014.03.021>

- Valer M, Bachèlery P, Schiano P (2017) The petrogenesis of plagioclase-ultraphyric basalts from La Réunion Island. *J Petrol* 58(4):675–698. <https://doi.org/10.1093/petrology/egx030>
- Walker GP (1958) Geology of the Reydarfjörður area, eastern Iceland. *Q J Geol Soc* 114(1–4):367–391. <https://doi.org/10.1144/gsjgs.114.1.0367>
- Webb BM, Streck MJ, McIntosh WC, Ferns ML (2019) The Littlefield Rhyolite and associated mafic lavas: bimodal volcanism of the Columbia River magmatic province, with constraints on age and storage sites of Grande Ronde Basalt magmas. *Geosphere* 15(1):60–84. <https://doi.org/10.1130/GES01695.1>
- White RS (1992) Magmatism during and after continental break-up. *Geol Soc Lond Special Publications* 68(1):1–16. <https://doi.org/10.1144/GSL.SP.1992.068.01.01>
- White R, McKenzie D (1989) Magmatism at rift zones: the generation of volcanic continental margins and flood basalts. *J Geophys Res: Solid Earth* 94(B6):7685–7729. <https://doi.org/10.1029/JB094iB06p07685>
- Wieser PE, Kent AJ, Till CB, Donovan J, Neave DA, Blatter DL, Krawczynski MJ (2023) Barometers behaving badly I: assessing the influence of analytical and experimental uncertainty on clinopyroxene thermobarometry calculations at crustal conditions. *J Petrol* 64(2):egac126. <https://doi.org/10.1093/petrology/egac126>
- Wolfenden E, Ebinger C, Yirgu G, Renne PR, Kelley SP (2005) Evolution of a volcanic rifted margin: Southern Red Sea, Ethiopia. *Geol Soc Am Bull* 117:846. <https://doi.org/10.1130/B25516.1>
- Wolff JA, Ellis BS, Ramos FC, Starkel WA, Boroughs S, Olin PH, Bachmann O (2015) Remelting of cumulates as a process for producing chemical zoning in silicic tuffs: a comparison of cool, wet and hot, dry rhyolitic magma systems. *Lithos* 236:275–286. <https://doi.org/10.1016/j.lithos.2015.09.002>
- Wright T, Sigmundsson F, Pagli C, Belachew M, Hamling IJ, Brandsdóttir B, Keir D, Pedersen R, Ayele A, Ebinger CJ, Einarsson P, Lewi E, Calais E (2012) Geophysical constraints on the dynamics of spreading centres from rifting episodes on land. *Nat Geosci* 5(4):242–250. <https://doi.org/10.1038/ngeo1428>
- Wynn JG, Roman DC, Alemseged Z, Reed D, Geraads D, Munro S (2008) Stratigraphy, depositional environments, and basin structure of the Hadar and Busidima Formations at Dikika, Ethiopia, in: *The Geology of Early Humans in the Horn of Africa*. Geological Society of America. [https://doi.org/10.1130/2008.2446\(04\)](https://doi.org/10.1130/2008.2446(04))

**Publisher's note** Springer Nature remains neutral with regard to jurisdictional claims in published maps and institutional affiliations.